University of BRISTOL

SCHOOL OF PHYSICS

Final Year Project Report

NAME:	Sophie Kelly
COURSE:	MSci Physics with a Year Abroad in a Modern Language
TITLE:	An investigation into refining the negative electron affinity and work function of boron-doped (110) diamond surfaces via oxygen-lithium treatments
YEAR OF SUBMISSION:	2026
SUPERVISOR:	Neil Fox & Jude Laverock
NUMBER OF WORDS:	~9000

School of Physics
Tyndall Avenue
Bristol BS8 1TL

Declaration

The diamond samples used in this project were grown in the diamond laboratory with assistance from Liam Cullingford and Catherine Monk. All measurements were performed in the NanoESCA facility under the guidance and aid of Jude Laverock. Practical experimental work was conducted collaboratively with my project partner, Joe Hynam, with both of us contributing equally to data acquisition. The analysis of the data and interpretation of results presented in this report was carried out by myself, informed by discussions with Joe Hynam, Neil Fox, and Ramiz Zulkharney.

AI Declaration

As part of the research described below, AI tools (ChatGPT) were used to proofread and aid in the clarification of concepts during research in accordance with the Project Unit's AI-use policy. AI tools were not used in the writing or production of this report.

Acknowledgements

I would like to express my sincere gratitude to Jude Laverock and Neil Fox for their invaluable support throughout this project. To Jude Laverock, for his guidance in the NanoESCA laboratory, as well as his knowledge of data acquisition, which were essential to both the experimental work and the interpretation of results. I am very grateful to Neil Fox for his advice and expertise in surface science, which ultimately shaped the direction of this research project. I would also like to thank Ramiz Zulkharnay for his assistance in data analysis and for the insightful discussions regarding surface functionalisation.

Finally, I would like to thank my project partner, Joe Hynam, for his hard work and support throughout the project. Our shared effort and discussions were fundamental to the progress of this work. It has been a pleasure working with you.

Abstract

A negative electron affinity (NEA) surface has been achieved on boron-doped single-crystal diamond (110) through controlled molecular oxygen and lithium functionalisation. The surface was prepared via iterative oxygen-lithium cycling, consisting of molecular oxygen exposure, lithium deposition, and thermal annealing. Following three cycles, a work function of **3.01 ± 0.05 eV** and an NEA of **−1.49 ± 0.05 eV** were obtained, representing a significant improvement over the hydrogen-terminated reference state. X-ray photoelectron spectroscopy (XPS) revealed that the evolution of surface chemistry is governed by the formation of C-O-Li bonding and EF-PEEM work function mapping confirmed that the resulting electronic properties are spatially uniform, indicating the formation of a homogeneous dipole-active surface. This work refines and contributes to the limited body of research on (110) diamond surfaces and highlights their potential for electron-emission-based energy conversion applications.

Contents

1. Introduction **7**

2. Theory **9**

2.1 Diamond Structure 9

2.1.1 Crystal Structure of Diamond 9

2.1.2 Electronic Structure of Diamond 10

2.1.3 Semiconductor Doping in Diamond 10

2.2 Electron Emission 11

2.2.1 Photoelectric Effect 11

2.2.2 Work Function 12

2.2.3 Thermionic Emission Theory 12

2.3 Electron Affinity 13

2.3.1 Negative Electron Affinity (NEA) 13

2.3.2 Surface Band Bending 14

2.3.3 Surface Dipole Formation 15

2.4 Surface Termination of Diamond 16

2.4.1 Hydrogen Termination 16

2.4.2 Oxygen Termination 16

2.4.3 Lithium Deposition 17

3. Experimental Methods **18**

3.1 Workflow 18

3.2 Diamond Growth 19

3.3 Ultra-High Vacuum (UHV) Procedures 20

3.3.1 Annealing 20

3.3.2 Non-Evaporable Getter (NEG) 21

3.3.3 Oxygen-Lithium Surface Functionalisation 21

3.4 The NanoESCA 22

3.4.1 X-ray Photoelectron Spectroscopy (XPS) 23

3.4.2. Ultraviolet Photoelectron Spectroscopy (UPS) 24

3.4.3 Photoemission Electron Microscopy (PEEM) 25

3.4.4 Spot Profile Analysis Low Energy Electron Diffraction (SPA-LEED) 26
3.5 Data Fitting and Models 27
3.5.1 CasaXPS 27
3.5.2 Python Code for UPS Fitting 28
3.5.3 Work Function Mapping in MATLAB 28
4. Results and Discussion **29**
4.1 Comparison of Hydrogen-Terminated Surfaces BS1 & BS3 29
4.1.1 Chemical Composition 29
4.1.2 Work Function Comparison 31
4.1.3 NEA Calculation 32
4.2 Surface Reconstruction SPA-LEED Analysis 33
4.3 Testing the Efficacy of the NEG 35
4.4 Oxygen-Lithium Cycling 37
4.4.1 O 1 s Surface Composition 37
4.4.2 Li 1s Surface Composition 38
4.4.3 Work Function and NEA 40
4.5 Progression Review 42
5. Conclusion **43**

1. Introduction

The development of long-lived, reliable energy sources is a key challenge in modern energy research [66], particularly for applications in extreme or inaccessible environments where conventional electrochemical batteries are unsuitable. Such batteries suffer from finite lifetimes and performance limitations under high temperatures or radiation exposure [1, 2]. These constraints have driven interest in alternative solid-state power sources such as thermionic converters and betavoltaic devices, which convert thermal or radiative energy directly into electricity and offer long operational lifetimes and stable power output [3].

The concept of direct energy conversion using semiconductors originates from early studies of the electron-voltaic effect in the mid-twentieth century, where energetic particle radiation was shown to induce charge separation in semiconductor junctions, generating electrical potential [4]. Subsequent advances in thermionic energy conversion highlighted the importance of surface electronic structure [1] while development of betavoltaic devices using beta-emitting radioisotopes demonstrated the feasibility of long-lived micro-batteries [5]. However, early devices based on silicon and germanium suffered from a limited efficiency and material degradation [6].

Interest in these technologies re-emerged with advances in wide-bandgap semiconductors like diamond which exhibits exceptional thermal conductivity [7, 8]. The performance of both thermionic and betavoltaic devices is critically determined by the electron emission efficiency of the emitter surface. This efficiency depends strongly on the surface work function and electron affinity of the emitting material [6]. Conventional thermionic emitting materials, retaining a work function ~3-5 eV require a minimum operating temperature of 1500 °C, which increases the risk of use and rate of surface degradation [9]. Diamond's wide bandgap allows for negative electron affinity (NEA), where the conduction band minimum of a material is raised above its vacuum level, allowing electrons to be emitted with minimal or no energy barrier [10, 11]. NEA has a direct influence on lowering the work function [12], enabling higher current densities at lower temperatures or under reduced radiation flux [13]. Consequently, engineering materials with stable, low work functions remains a key objective for next-generation energy harvesting devices.

The development of chemical vapour deposition enabled the growth of high-purity synthetic diamond with controlled doping, making diamond-based energy conversion devices technologically viable [14]. Within this project, boron is used as a chemical dopant. Boron-doped diamond (BDD) was the first material shown to exhibit true NEA [15] and BDD electrodes are reported to be more resistant and chemically inert under extreme conditions, making them useful in industrial applications [16]. Unlike many conventional semiconductors, diamond possesses no native oxide layer, allowing its surface electronic properties to be deliberately tailored through chemical termination [10]. Hydrogen (H) termination is a common method of producing NEA, with reported values of -1.0 ± 0.1 eV for (110) surfaces [17]. However, its practical use is limited by thermal and environmental instability [18, 19], motivating the search for alternative terminations capable of delivering both large and stable NEA [20].

Metal-oxygen functionalisation has emerged as a leading approach to address this challenge. In particular, oxygen-lithium (O-Li) terminations produce some of the largest NEA values reported for diamond [21], with density functional theory predicting values up to −3.5 eV for the (100) diamond surface [22] and experimental studies demonstrating NEA of approximately −2.4 eV [23]. The physical origin of this behaviour lies in the formation of a strong surface dipole: oxygen termination provides a chemically stable interface [24], while lithium adsorption induces charge redistribution that lowers the vacuum level relative to the conduction band [9].

Recently, a novel molecular oxygen oxidation technique for single-crystal (100) diamond (SCD) has achieved 90% surface oxygen coverage and demonstrated an NEA of −1.68 eV following lithium deposition on a (100) diamond surface, outperforming conventional UV-ozone treatment (−1.31 eV) [20]. Importantly, although some degradation occurred under ambient exposure, the NEA was shown to be recoverable (−1.56 eV) upon reactivation, establishing molecular oxygen termination as a scalable and high-performance route to stable NEA surfaces [20].

Additional investigation involving the deposition of lithium onto the molecular-oxygen-treated diamond (110) surface is also significant to this report. The introduction of cyclic O-Li treatments, combined with controlled annealing to improve surface uniformity and electronic performance, achieved an NEA of -1.5 ± 0.1 eV using molecular oxygen termination, compared to -0.8 ± 0.1 eV for ozone-treated surfaces [25]. This work further demonstrated a reduction in work function of 3.8 ± 0.5 eV to 3.5 ± 0.3 eV after the repeated O-Li treatments [17]. These results reinforced the importance of both termination method and iterative surface processing in optimising NEA and highlighted the (110) surface as a promising but relatively unexplored orientation.

This project directly aims to build upon the work of University of Bristol research projects [17, 25] by further investigating and refining the role of controlled surface functionalisation in determining the electronic properties of boron-doped SCD (110) surfaces. The aim is to explore reproducible methods for achieving low work function surfaces and stable NEA conditions suitable for electron-emission-based energy conversion through sequential molecular oxygen termination and lithium deposition, with particular emphasis on O-Li cycling as a means of stabilising surface dipoles and enhancing uniformity.

Over the course of this project, I have developed expertise in surface engineering and electronic structure analysis, in addition to spectroscopic and microscopy techniques using ultra-high vacuum (UHV) instrumentation to demonstrate how controlled surface chemistry can tailor material properties for energy applications.

2. Theory

2.1 Diamond Structure

2.1.1 Crystal Structure of Diamond

Diamond is a crystalline allotrope of carbon (C) in which each atom is tetrahedrally coordinated (sp^3) to four neighbours through strong covalent bonds. This produces a three-dimensional diamond cubic structure (space group Fd-3m), as shown in Figure 1, consisting of two interpenetrating face-centred cubic structures offset along the body diagonal [26].

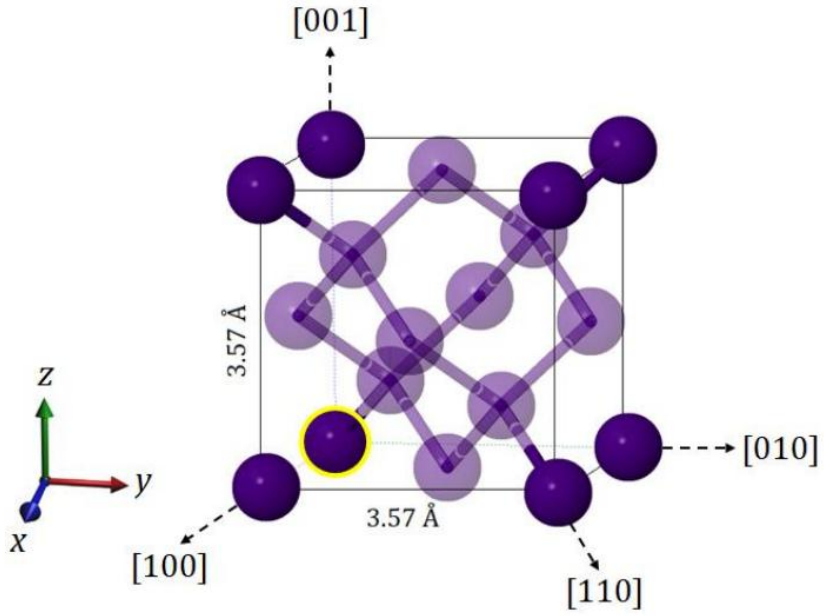

Figure 1: Crystal structure of cubic diamond, showing the tetrahedrally bonded carbon lattice within a conventional unit cell. The origin atom is highlighted in yellow, while dashed arrows denote surface orientation directions. Reproduced from [27].

When the crystal is truncated to form a surface, unsatisfied 'dangling' bonds are introduced, increasing surface energy and reactivity [28]. As a result, diamond surfaces reconstruct or terminate chemically to minimise this energy. The atomic arrangement of these surface planes plays a critical role in determining both chemical stability and electronic behaviour.

The three principal orientations are the (100), (110) and (111) diamond surfaces. Figure 2 shows while the (100) surface exhibits a cubic construction and the (111) surface can display more densely packed triangular reconstructions, the (110) surface is structurally distinct, consisting of rows of atoms arranged in a zig-zag chain configuration [29]. This results in a comparatively open surface with easier access to carbon sites, allowing more direct interaction between terminating species and surface carbon atoms [30]. This makes the (110) surface structure particularly well suited for controlled studies of surface termination, in addition to its lack of reconstruction up to 1300K, unlike the (100) and (111) orientations [23].

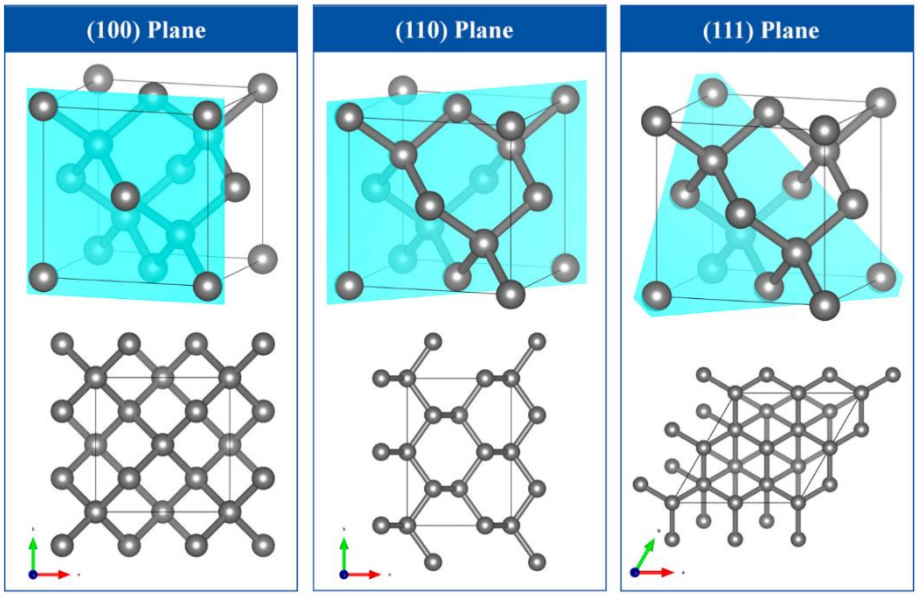

Figure 2: Diamond lattice structures for the (100), (110), and (111) orientations. Top: 3D unit cells with the cutting planes illustrated in cyan. Bottom: 2D atomic arrangement from a perpendicular view to the planes above. Reproduced from [30].

Recent studies have demonstrated that boron-doped (110) diamond can support strong and reproducible NEA following oxygen-lithium treatment, with measured values approaching −1.5 eV and significant reductions in work function after repeated treatment cycles [25]. These results highlight the sensitivity of the (110) surface to termination chemistry, as well as its suitability for achieving spatially uniform electronic properties.

2.1.2 Electronic Structure of Diamond

Diamond is an ultra-wide bandgap semiconductor with an indirect bandgap of approximately $E_g = 5.47eV$ [31]. In intrinsic diamond, the Fermi level lies close to mid-gap, resulting in an extremely low intrinsic carrier concentration at room temperature. Consequently, undoped diamond behaves as an electrical insulator. To achieve effective electrical conductivity, controlled doping is therefore required to introduce mobile charge carriers [32] and to shift the Fermi level to a position more favourable for electron emission.

2.1.3 Semiconductor Doping in Diamond

In this project, the relevant dopant is boron, which introduces p-type conductivity. When a boron atom substitutes for carbon in the diamond lattice, it brings only three valence electrons rather than four. This creates an acceptor state within the band structure, located approximately 0.37 eV above the valence band maximum [32]. This acceptor level can accept an electron from the valence band, leaving behind a mobile hole seen in Figure 3(a).

Boron doping therefore increases the hole concentration, turning the diamond into a p-type semiconductor and shifting the Fermi level downward, toward the valence band [33]. This shift directly affects the work function as it alters the energy required to remove an electron from the material. Boron is a particularly useful materiel

to work with as its doped electrodes exhibit high chemical stability with a large potential window due to its high carrier concentration shown in Figure 3(b) [6, 34].

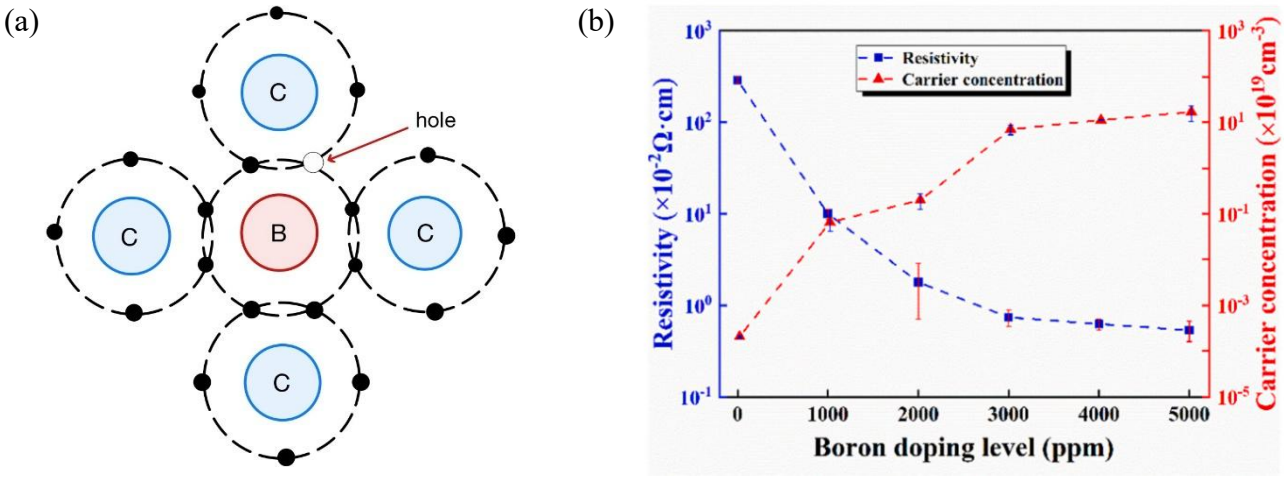

Figure 3: (a) Substitutional boron doping in the diamond lattice. A boron atom replaces a carbon atom in the lattice, introducing an acceptor state and creating a hole, which enables p-type conductivity. (b) Inverse relationship dependence of electrical resistivity and carrier concentration on boron doping level in BDD. At high doping levels, both quantities approach saturation due to reduced dopant activation and increased defect scattering. Reproduced from [33].

2.2 Electron Emission

2.2.1 Photoelectric Effect

Photoemission spectroscopy is based on the photoelectric effect, explained quantitively by Einstein in 1905 via an energy-balance model for election emission [35]. In this process, depicted in Figure 4, photons incident on a material transfer their energy to electrons within the material. If the photon energy is sufficient to overcome both the binding energy of the electron and the surface escape barrier (work function), the electron can be emitted into vacuum [35].

The kinetic energy of the emitted electron is given by:

$$E_k = h\nu - E_b - \Phi \text{ [36].} \quad (1)$$

$h\nu$ is the photon energy, E_b is the binding energy of the electron within the material, and Φ is the work function of the surface [35]. By measuring the kinetic energy of emitted electrons, it is therefore possible to determine their binding energies and obtain information about the electronic structure of the material [37].

Because electrons travelling through a solid have a relatively short mean free path, ~0.1-0.8 nm at ~30-100 eV, only electrons originating from the top few nanometres of the surface can escape without inelastic scattering

[38]. Photoemission spectroscopy is therefore inherently surface sensitive, making it particularly well suited to studying surface chemistry and electronic properties.

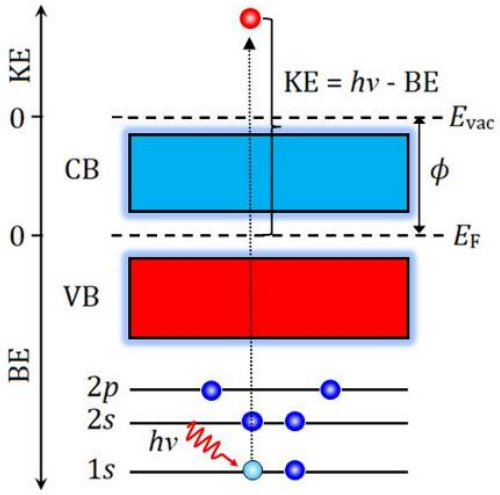

Figure 4: Schematic of the photoemission process. An incident photon of energy hv excites a core-level electron, which is emitted with kinetic energy determined by its binding energy and the material work function, leaving a core hole in the atomic structure. Reproduced from [27].

2.2.2 Work Function

The work function is the minimum energy required to remove an electron from the material to the vacuum level, E_{vac}, starting from the Fermi level, E_F. It is defined as:

$$\Phi = E_{vac} - E_F \text{ [23].} \tag{2}$$

The vacuum level represents the energy of an electron that is just outside the material and free from its binding potential. It is therefore the reference level to which emitted electrons must rise.

2.2.3 Thermionic Emission Theory

Thermionic emission is the process by which electrons acquire sufficient thermal energy to escape from a material into vacuum [39]. In a classical picture, electrons within the material have a thermal energy distribution. A small fraction in the high-energy tail of that distribution possess enough energy to overcome the surface barrier and be emitted [9]. The rate at which this occurs depends on the height of that barrier, i.e. the work function.

For thermionic emission, the emitted current density J is described by the Richardson-Dushman equation:

$$J = A^* T^2 \exp\left(-\frac{\Phi}{k_B T}\right). \tag{3}$$

A^* is the effective Richardson constant, T is the temperature, and k_B is Boltzmann's constant [9, 40]. The exponential dependence on Φ highlights the importance of minimising the work function as even a modest reduction can produce a significant increase in emission at a given temperature. Consequently, engineering a material with a lower work function can also achieve a given current density at much lower operating temperatures [41].

2.3 Electron Affinity

For semiconductors, another equally important quantity is the electron affinity, defined as:

$$\chi = E_{vac} - E_{CBM}, \tag{4}$$

where E_{CBM} is the energy of the conduction band minimum [9]. The conduction band minimum is the lowest-energy state within the conduction band into which electrons must be promoted to ultimately be emitted [10].

Surface chemistry is used to modify both the work function and electron affinity, but in slightly different ways. The work function depends on the position of the Fermi level and therefore on doping [10]. The electron affinity depends on the conduction band minimum and therefore on how the surface vacuum level sits relative to the band structure [40].

2.3.1 Negative Electron Affinity (NEA)

A surface exhibits NEA when the vacuum level lies below the conduction band minimum, $\chi < 0$, seen in Figure 5(b) [9].

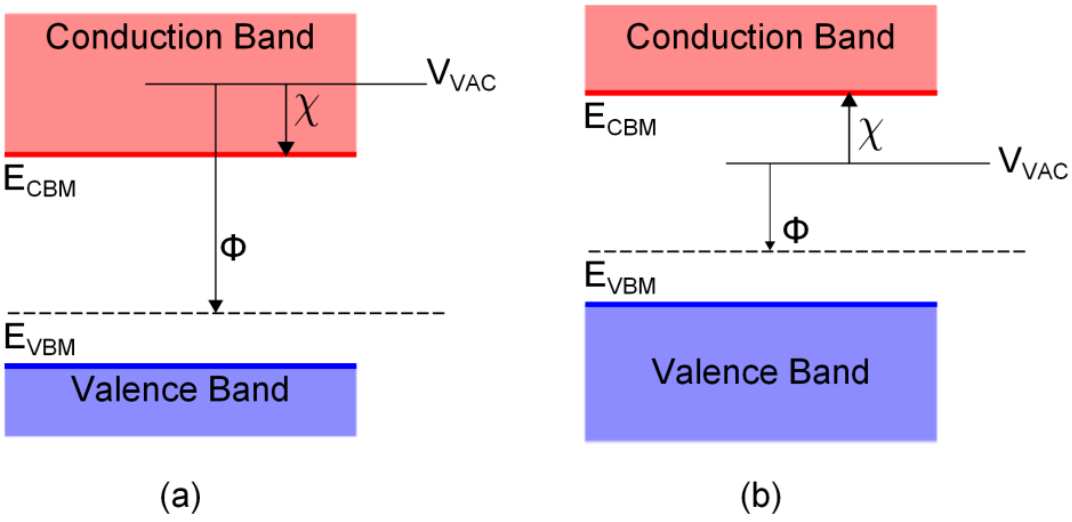

Figure 5: Energy band diagrams illustrating (a) positive electron affinity (PEA), where the vacuum level lies above the conduction band minimum; (b) true NEA, where the vacuum level lies below the conduction band minimum, enabling barrier-free electron emission. Reproduced from [23].

Under this condition, an electron that reaches the bottom of the conduction band does not face an additional barrier to escape into vacuum. Instead, it can be emitted directly. This is an extraordinary property because in most materials the vacuum level lies above the conduction band minimum, $\chi > 0$, as shown in Figure 5(a) so some energy barrier remains even after an electron has reached the conduction band [11].

For thermionic devices, this offers two important advantages. First, it allows emission to occur at lower temperature, reducing thermal stress and improving materials compatibility. Second, it increases the potential efficiency of the emitter, since a larger fraction of thermally excited electrons can contribute to useful current rather than remaining trapped below the surface barrier. Hence there is a continued focus on stabilising large-NEA diamond terminations for thermionic emitters [20].

2.3.2 Surface Band Bending

The discussion above treats the band edges as though they were flat right up to the surface. In reality, semiconductor surfaces often exhibit band bending, shown in Figure 6, due to charge redistribution near the surface [11]. This arises when surface states, adsorbates or defects trap charge and alter the local electrostatic potential [9]. Because the bulk Fermi level must remain continuous through equilibrium, the conduction and valence band edges shift (bend) relative to it near the surface to maintain charge balance.

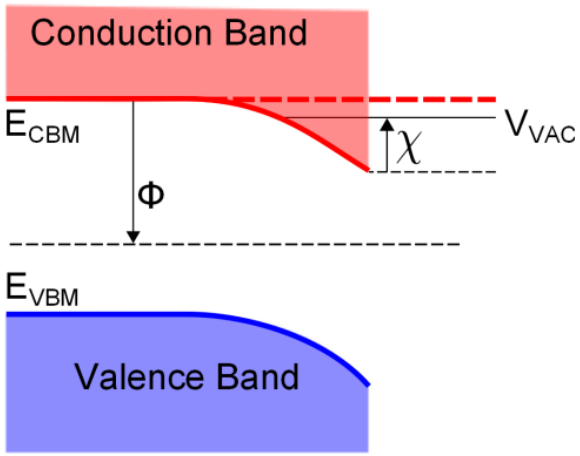

Figure 6: Band diagram showing effective NEA, where band bending near the surface locally lowers the vacuum level to permit emission despite a non-NEA bulk alignment. Reproduced from [23].

The electrostatic potential V(x) governing this behaviour is described by Poisson's equation:

$$\frac{d^2V}{dx^2} = -\frac{\rho(x)}{\varepsilon}, \tag{5}$$

where ρ(x) is the local charge density and ε is the permittivity [42]. This equation states that spatial variations in electric potential are produced by charge density. Band bending is therefore important because it can either impede or assist electron transport near the surface and alter the local carrier population [9].

Surface chemistry also induces charge transfer that changes the near-surface electric field and bends the bands [11]. The measured work function is therefore influenced by both the vacuum-level shift from surface dipoles and the band-edge shifts caused by electrostatics.

2.3.3 Surface Dipole Formation

Another important theoretical idea in this project is that surface chemistry changes electron emission by creating surface dipoles. A surface dipole arises whenever there is spatial separation of positive and negative charge at the surface [43]. This dipole generates an electrostatic potential step, which shifts the vacuum level relative to the underlying band structure, modifying the work function and electron affinity [40].

There are two types of surface dipole in diamond. The first is the atom-centred dipole. This arises when charge is transferred between the terminating species and the surface carbon atom, so that one atom becomes partially positive and the other partially negative. The dipole moment is mainly associated with the positions of the atomic centres and the separation of their partial charges [43].

The second is the bond-centred dipole. In this case, the relevant charge asymmetry is associated more directly with the polarised covalent bond itself. Density functional theory (DFT), modelled in Figure 7, has shown that both the magnitude and direction of the resulting vacuum level shift depend on the electronegativity and bonding configuration of the terminating species [23]. Consequently, different terminations produce distinct electronic responses.

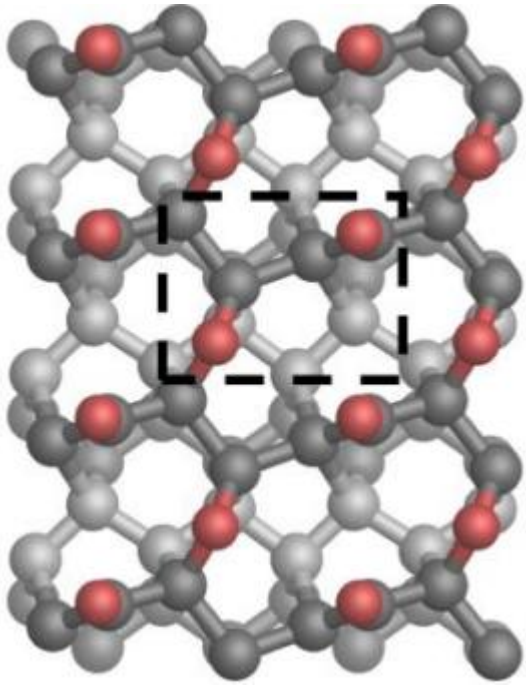

Figure 7: DFT model of the lowest-energy oxygen bonding configuration on the diamond (110) surface. Oxygen atoms form stable surface functional groups that modify the surface dipole and electronic structure. Unit cell indicated by box. Reproduced from [44].

2.4 Surface Termination of Diamond

2.4.1 Hydrogen Termination

Hydrogen termination occurs when hydrogen atoms bond to the dangling bonds of surface carbon atoms, forming a stable surface following chemical vapour deposition (CVD) growth in a hydrogen-rich plasma [31]. Termination, shown in Figure 8, stabilises the surface by saturating reactive dangling bonds and preventing graphitisation [45].

Electronically, hydrogen termination is important because it creates an outward surface dipole, pictured in Figure 9(a), that shifts the vacuum level downward relative to the conduction band. This produces NEA [31], enabling efficient electron emission. However, purely hydrogen-terminated diamond surfaces are known to lose conductivity and NEA under UHV conditions [46]. In this project it therefore provides as a well-defined reference state for evaluating subsequent surface modifications.

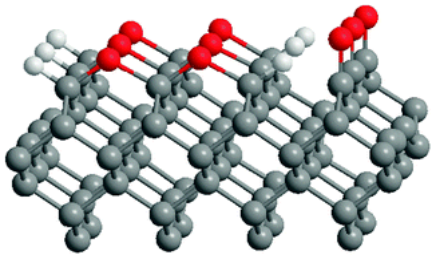

Figure 8: Idealised structures for hydrogen- and oxygen-terminated diamond surfaces. Gray spheres represent carbon atoms; red and white spheres represent surface bound oxygen and hydrogen atoms respectively. Reproduced from [47].

2.4.2 Oxygen Termination

Oxygen termination occurs when oxygen-containing species bond to surface carbon atoms, forming polar C-O based configurations such as ether C-O-C, ketone C=O or hydroxyl C-OH groups, shown in Figure 9(b) [44]. Due to the high electronegativity of oxygen, these bonds induce inward surface dipoles that shift the vacuum level upward relative to the conduction band.

As a result, oxygen-terminated diamond typically exhibits PEA, increasing the energy barrier for electron emission compared to hydrogen-terminated surfaces [44]. However, oxygen termination plays a critical role in surface engineering. The chemically stable and electronegative nature of oxygen provides well-defined adsorption sites for subsequent chemical functionalisation [24]. In this project, oxygen treatment therefore acts as an intermediate step, establishing a chemically prepared platform onto which lithium can be deposited.

2.4.3 Lithium Deposition

Lithium deposition was chosen to expand on recent research [17, 25], as it provides a means of significantly reducing the work function through strong charge donation to the surface [9]. As an alkali metal, lithium readily transfers its valence electron, creating an outward surface dipole, as seen in Figure 9(c), that lowers the vacuum level, inducing NEA and ultimately lowering the work function [21, 22].

The specific mechanism explored in this project is the formation of O-Li dipoles on an oxygen-terminated diamond surface. Here, oxygen provides chemically stable electronegative sites that bind lithium, while lithium donates positive charge [23]. Experimental investigations have shown that method of lithium adsorption outperforms hydrogen termination [24, 48] by producing a stable and strongly bound surface capable of generating NEA values as low as -3.89 eV under simulation [23].

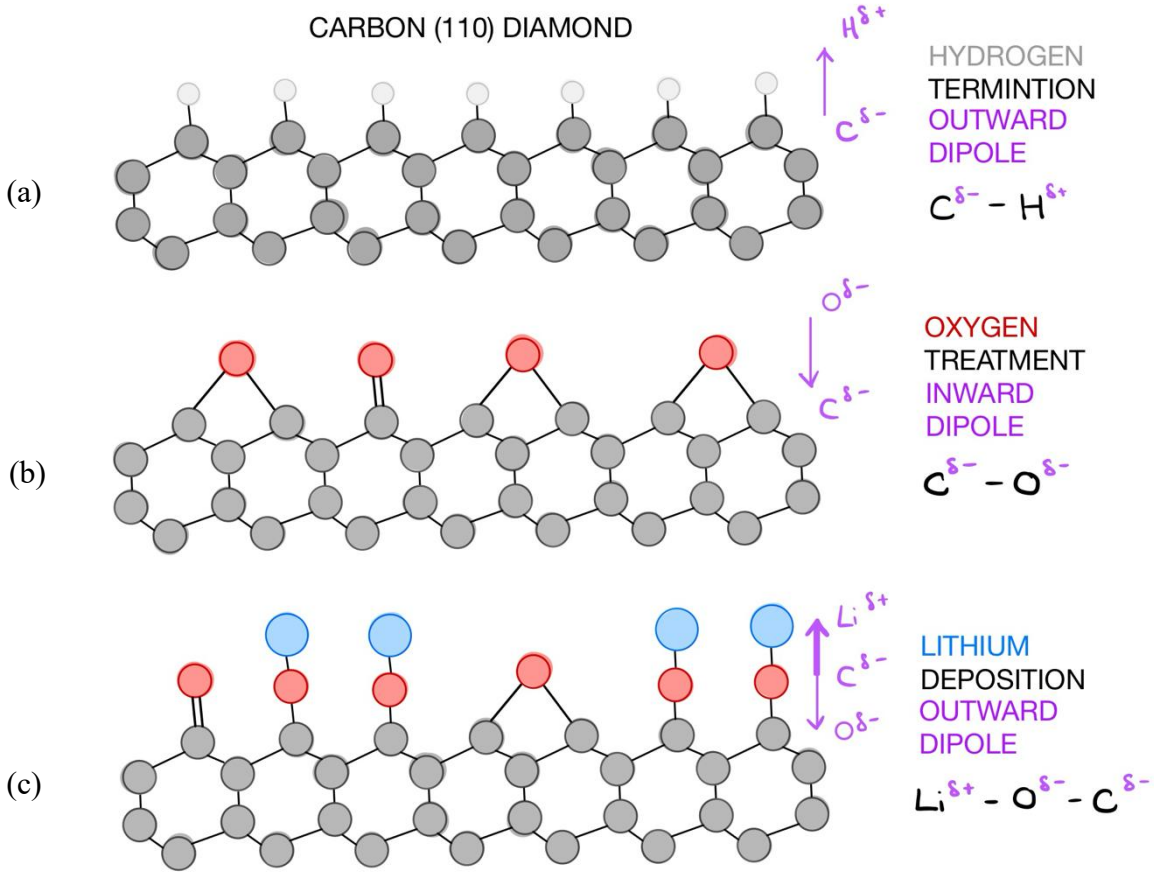

Figure 9: Schematic of the stepwise surface functionalisation of the (110) BDD, showing the transition from (a) hydrogen termination to (b) oxygen termination and (c) subsequent lithium adsorption, illustrating the evolution of surface dipoles and the transition between PEA and NEA states.

3. Experimental Methods

3.1 Workflow

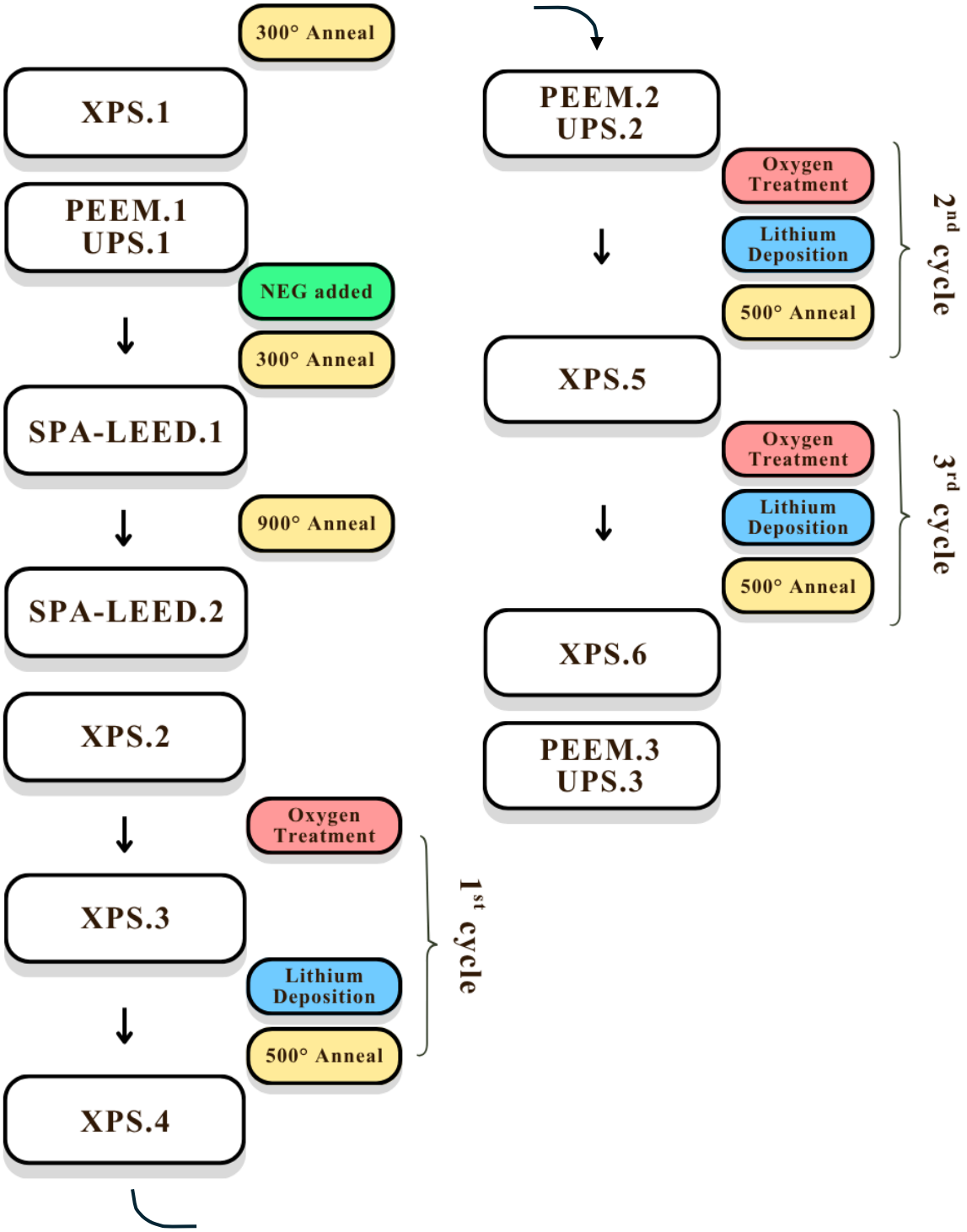

Workflow: Overview of the experimental sequence performed on BS1, including iterative oxygen-lithium surface functionalisation cycles. XPS was used to monitor surface chemistry evolution, while PEEM and UPS evaluate changes in electronic structure and work function. BS2 was deemed unusable after a sudden discharge in the analysis chamber. Only XPS.1, PEEM.1, and UPS.1 measurements were obtained for BS3 before it fell out of its molybdenum hold.

3.2 Diamond Growth

Three 6.8 x 3.3 mm (110) diamond samples purchased from Element Six Technologies Ltd. (product code 145-500-0573) were used in this project and named BS1, BS2, and BS3, respective of their order of growth. These three boron-doped samples were identically grown using microwave plasma chemical vapour deposition (MPCVD), a 3kW microwave plasma system operating at ~900 °C, capable of producing high-quality diamond films at growth rates up to 20 μm h^{-1} over a substrate area of approximately 2 cm^2.

The physical basis of MPCVD, illustrated in Figure 10, lies in plasma generation by microwave excitation. A low-pressure gas mixture consisting of 300 sccm of H_2, 12.5 sccm of CH_4, and 0.5 sccm of B_2H_6 was introduced into the growth chamber and irradiated with microwave power of 1.2kW at a pressure of 120 Torr for a 1-hour duration. The oscillating electromagnetic field accelerates free electrons within the chamber. These energetic electrons collide with gas molecules, causing ionisation, excitation, and dissociation [49]. Once a sufficient density of charged and excited species is established, a plasma is sustained above the substrate.

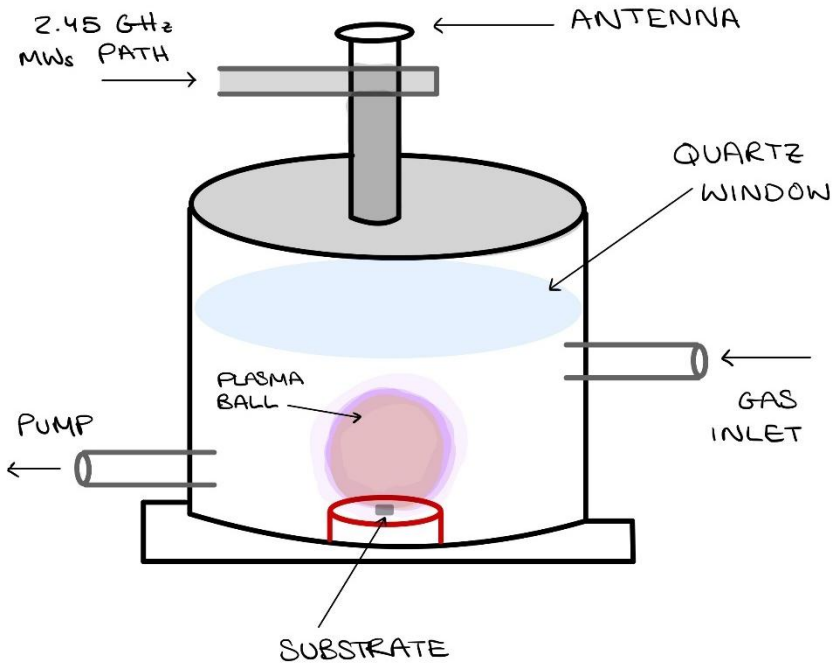

Figure 10: Diagram of the MPCVD reactor chamber used for diamond growth. Microwave radiation is introduced into the chamber to sustain a plasma by accelerating electrons into a mix of precursor gases. The plasma is positioned above the substrate to enable controlled diffusion of reactive species while minimising ion bombardment and thermal damage. Gas flow and chamber pressure are regulated via a pumping system, and the quartz window isolates the microwave source from the plasma region. Adaptation from [27].

In diamond deposition, Figure 11(b) shows that hydrogen acts as the main plasma-supporting gas and favours the stabilisation and growth of sp^3-bonded diamond [23]. Hydrogen also terminates dangling bonds on the growing surface, helping to stabilise the metastable diamond phase [45]. In the plasma, methane is dissociated into reactive carbon-containing radicals, the most important of which is generally regarded to be CH_3, which serves as the carbon source [45]. This radical is adsorbed at reactive surface sites and participates in step-flow growth on the diamond surface. For the purpose of this project, boron doping was introduced during growth via diborane (B_2H_6) in order to produce p-type conductivity in the form on BDD, seen in Figure 11(a).

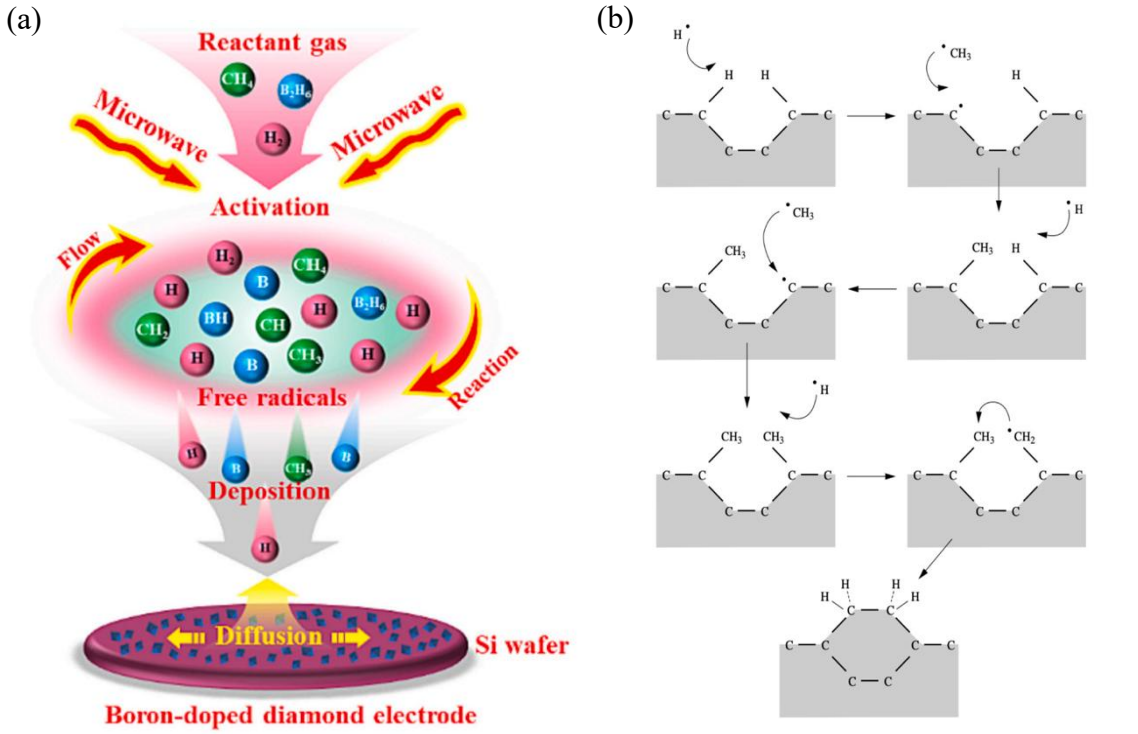

Figure 11: Schematic of the deposition process involved in MPCVD (a) of BDD. Microwave excitation of a $CH_4 - H_2 - B_2H_6$ gas mixture generates reactive radicals (e.g. CH_3, H, B-species) through ionisation, excitation, and dissociation. Reproduced from [33]. These species then undergo (b) surface reactions, leading to diamond growth on the substrate. Reproduced from [26].

3.3 Ultra-High Vacuum (UHV) Procedures

3.3.1 Annealing

Once transferred into the NanoESCA, the diamond samples required careful thermal preparation before surface analysis could be performed. Annealing serves several purposes in UHV surface science. First, it removes weakly adsorbed contaminants such as water, hydrocarbons and adventitious carbon that accumulate during air exposure and handling [29]. Second, different temperatures can desorb specific surface species depending on their chemical binding energies. Third, it may aid in the rearrangement of a more ordered surface reconstruction, improving the quality of diffraction and spectroscopy measurements [50].

The initial 300 °C anneal was used as a cleaning step to remove weakly bound contamination [51] while preserving the pre-grown hydrogen termination as far as possible. This was essential because the hydrogen-terminated surface formed the baseline against which later functionalisation states were compared.

The later 900 °C anneal had a very different role. At this elevated temperature, more strongly bound species can desorb, removing the layer of hydrogen termination [51]. Such a treatment was therefore useful to reset the surface before introducing a new termination chemistry. High-temperature annealing also helps reveal whether the surface can recover an ordered structure, something tested in the project using SPA-LEED.

Intermediate anneals around 500 °C between O-Li cycles served a more local cleaning and stabilisation role. After oxygen treatment and lithium deposition, such anneals can drive desorption of weakly bound residual species prepare the surface for the next XPS measurement.

3.3.2 Non-Evaporable Getter (NEG)

A major challenge in UHV experiments on hydrogen-sensitive surfaces is that hydrogen is difficult to eliminate completely from the chamber atmosphere. Because hydrogen is light, mobile and often present as a residual gas, it can re-adsorb on reactive surfaces and modify their termination state [52]. As the aim of this project is to produce a homogeneous O-Li surface, uncontrolled background hydrogen is especially problematic.

To mitigate this, the project introduced a NEG: a material often based on a zirconium-containing alloy, that actively sorbs reactive residual gases once activated [53]. Unlike cryogenic or passive pumping, a getter chemically binds gases such as hydrogen and water to its surface or into its bulk [53].

The first advantage of the NEG is improving the effective cleanliness of the vacuum chamber, reducing the rate at which reactive gases recontaminate the sample surface. This is particularly important after high-temperature annealing, when the freshly cleaned surface may be highly reactive. Second, it stabilises interpretation of the measurements. By actively reducing residual hydrogen, the NEG helps preserve the distinction between deliberate surface functionalisation steps.

3.3.3 Oxygen-Lithium Surface Functionalisation

A defining feature of this project is the use of repeated O-Li treatment cycles to incrementally build a controlled surface dipole layer. Rather than assuming a single oxygen treatment followed by lithium deposition would yield the optimal surface, the functionalisation was treated as a progressive process, with XPS used after each cycle to monitor the evolution of C-O and O-Li bonding.

Molecular oxygen was selected to produce a more uniform and controlled oxidation, providing consistent adsorption sites for lithium. As BS1 was chosen to undergo this process, the sample was exposed to molecular oxygen at a pressure of 1×10^{-2} mbar for 5 minutes. Lithium was subsequently deposited at a temperature of 485 °C at a current of 2.85A for 203 seconds. Previous data acquired at the NanoESCA suggests this forms ~ 2/3 monolayer (ML) coverage (two lithium atoms for every three carbon atoms). This was purposely chosen to be higher than the ~1/2 monolayer used by [25] to increase dipole density and improve surface uniformity while avoiding clustering associated with higher coverages.

Three O-Li cycles are recognised to be sufficient to reach a near-saturated and stable surface state [17, 25]. XPS changes became minimal, indicating that additional cycles would not significantly increase O-Li coverage but instead risk disorder or desorption effects. Three iterative treatments therefore enabled convergence toward a homogeneous dipole layer without over-processing the surface.

3.4 The NanoESCA

The experimental measurements described in this project were performed using a NanoESCA spectromicroscopy system, shown in Figure 12, which integrates several complementary surface analysis techniques within a single UHV environment.

The NanoESCA system combines XPS, UPS, PEEM and LEED capabilities with high spatial and energy resolution. Operating under UHV conditions typically below 10^{-10}mbar [54], the instrument uses monochromatic vacuum-ultraviolet light sources and an aberration-corrected hemispherical electron analyser. Typical performance parameters include an energy resolution of 19 meV and lateral image resolution of 13 nm with field of view (FOV) down to 3 microns [17]. These capabilities allow detailed investigation of local variations in electronic structure across the surface.

Because all measurements are performed within the same vacuum environment, the NanoESCA system allows sequential surface treatments and characterisation without exposing the sample to atmospheric contamination.

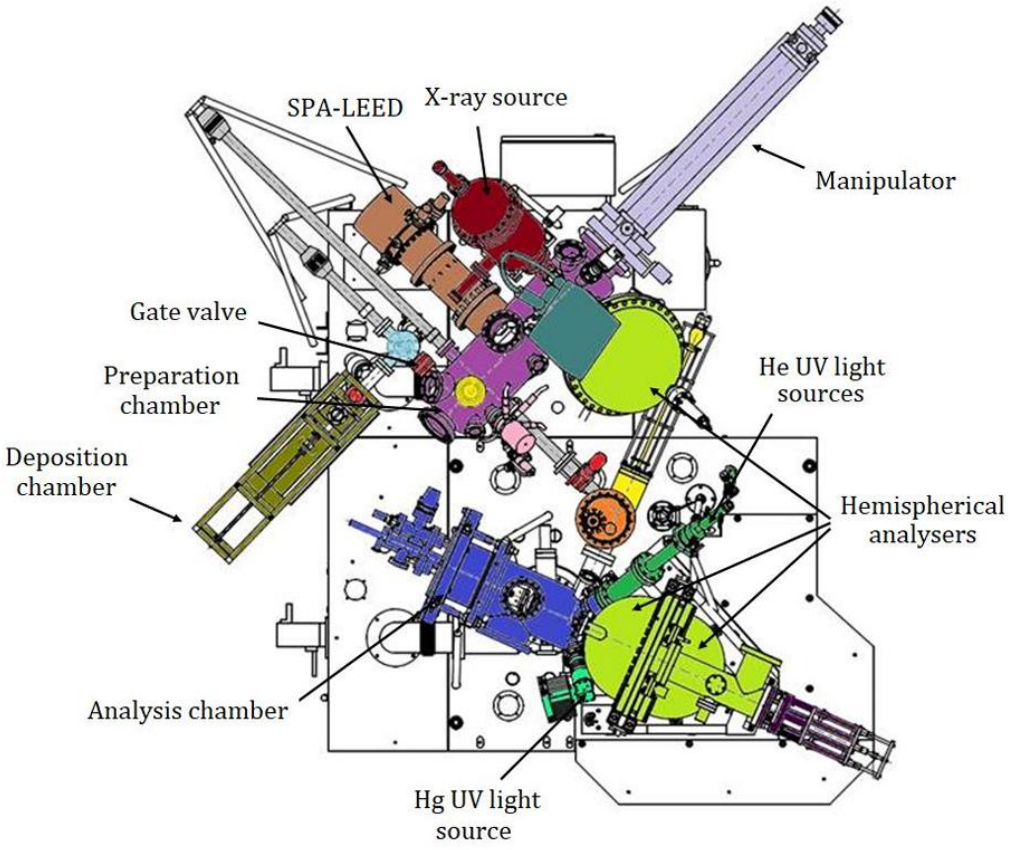

Figure 12: Schematic of the Bristol NanoESCA UHV system used for in situ surface preparation and analysis. Reproduced from [27].

3.4.1 X-ray Photoelectron Spectroscopy (XPS)

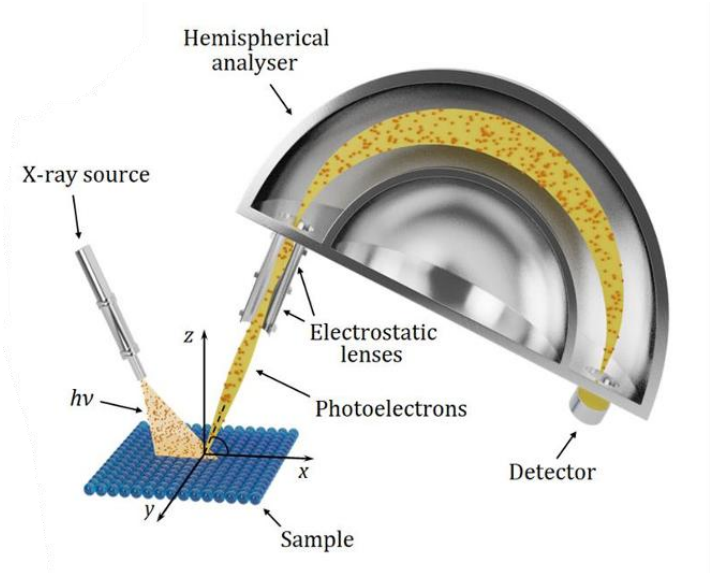

Figure 13: Schematic of the XPS instrumentation layout, showing X-ray excitation of the sample and subsequent emission of photoelectrons, which are focused by electrostatic lenses. The hemispherical analyser energy-selects emitted electrons by allowing only those with a defined kinetic energy to follow a stable trajectory to the detector, enabling precise determination of their energy distribution. Reproduced from [27].

XPS is one of the most widely used techniques for determining the chemical composition of surfaces to a depth of ~10 nm [25]. Figure 13 describes the XPS process; high-energy X-ray photons were used to excite core-level electrons from atoms within the material using a monochromatic Al Kα source (1486.7 eV). The binding energy of these electrons is determined from their measured kinetic energy using Equation (1) [36]. Because the binding energies of core electrons are characteristic of specific elements, XPS allows identification of the atomic species present on the surface [55].

In addition to elemental identification, XPS also provided information about the small shifts in binding energy, known as chemical shifts, which occur when atoms are bonded in various chemical configurations as shown in Figure 14(a, b). Through fitting software, peak shape and position were used to determine these functional groups, their binding energies, and their ratios on the surface.

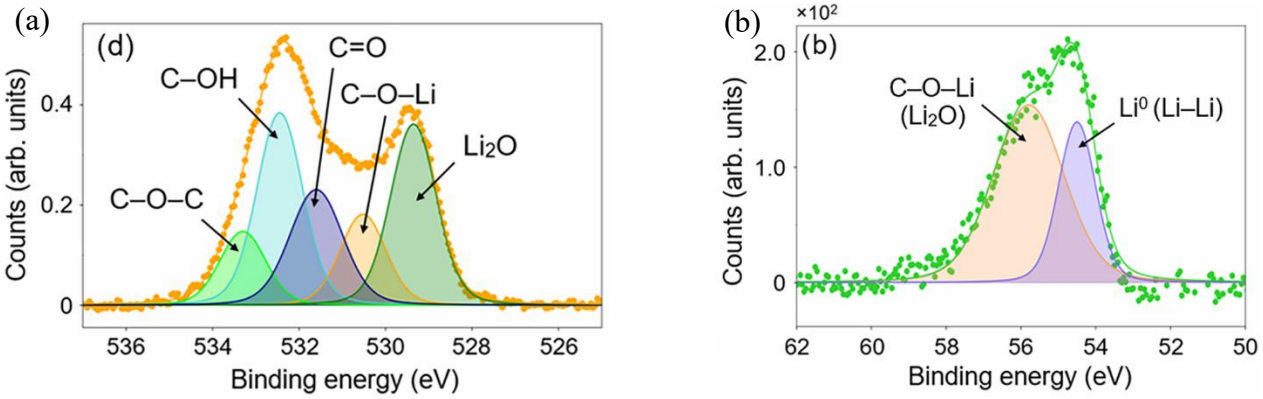

Figure 14: Example XPS analysis of lithiated, molecular oxygen-terminated (100) SCD surfaces. (a) Deconvoluted fit of the O 1s spectrum measurements showing contributions from multiple oxygen bonding configurations. (b) Fitted Li core-level spectrum illustrating contributions from O-Li bonding following lithium deposition. After [20].

For diamond surfaces, XPS is particularly valuable for identifying the presence of different surface terminations [20]. By taking survey scans with a pass energy of 50 eV and high-resolution scans centred on the C 1s, O 1s and Li 1s core-level peaks at a pass energy of 20 eV, it was possible to analyse and track how the surface composition changed throughout the functionalisation process.

3.4.2. Ultraviolet Photoelectron Spectroscopy (UPS)

UPS, on the other hand, uses lower-energy UV photons to probe valence band and near-Fermi level electronic states at around 2 nm from the surface. Because valence electrons are directly involved in chemical bonding, UPS provided important measurements of the surface work function and electron affinity, utilising He I radiation ($h\nu = 21.2\ eV$) to determine the material's surface properties [23, 56].

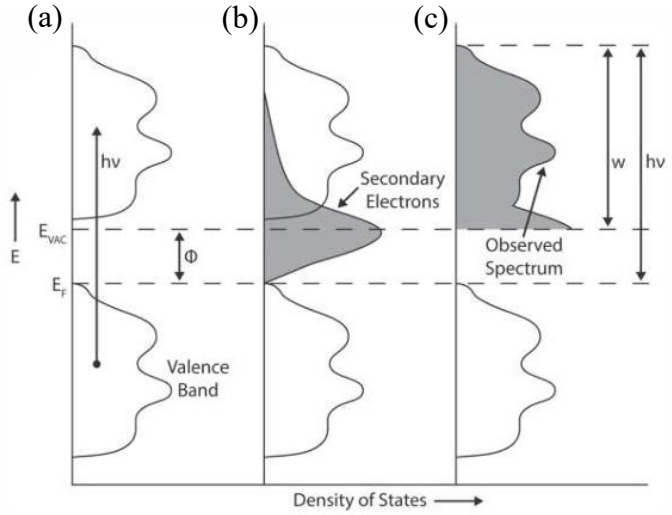

Figure 15: Schematic illustration of the UPS processes. a) UV photons ($h\nu$) excite electrons from occupied valence states to energies above vacuum level. b) During transport to the surface, some electrons undergo inelastic scattering, forming secondary electrons. c) The resulting spectrum consists of both photoelectrons and secondary electrons, from which the work function can be determined. Reproduced from [56].

The work function can be determined by measuring the secondary electron cutoff, E_{SECO}, in the photoelectron spectrum, shown by the process in Figure 15(a, b, c), and by applying the following equation:

$$\Phi = h\nu - (E_{SECO} - E_F). \tag{6}$$

To consequently determine electron affinity, E_g is used alongside the valence band offset ξ, to formalise the relation:

$$\chi = \Phi + \xi - \mathrm{E_g};$$
$$\xi = E_F - E_{VBM}.$$

(7)
(8)

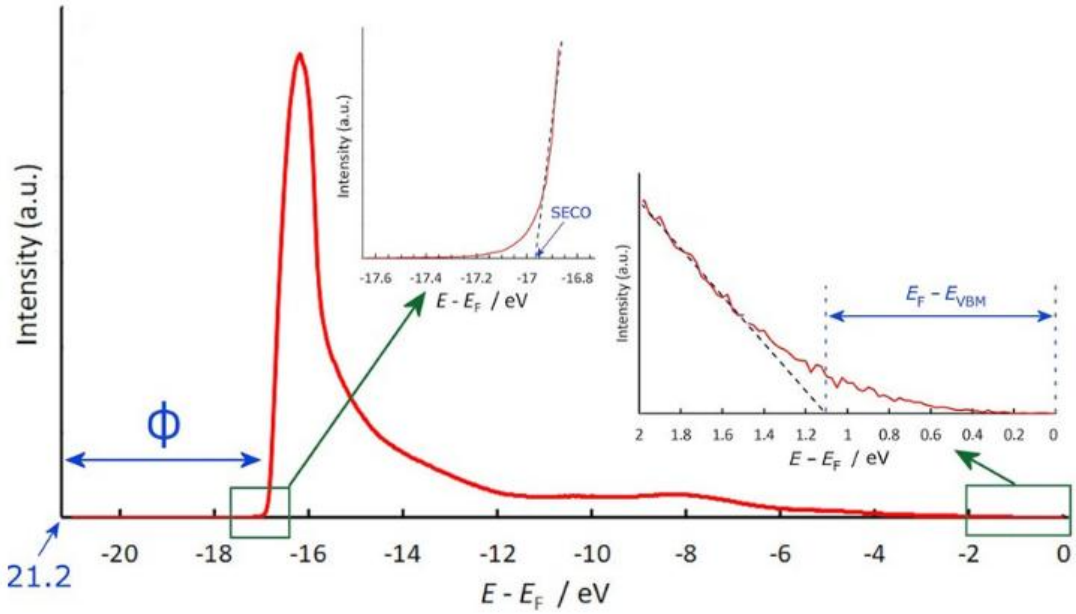

Figure 16: UPS spectrum showing extraction of work function and valence band position. The secondary electron cut-off (SECO) is determined by linear extrapolation of the low kinetic energy edge, yielding equation (6), while the valence band maximum is obtained from extrapolation of the valence band onset [57]. The presence of a strong secondary electron peak indicates NEA. Reproduced from [10].

In this project, UPS measurements are crucial in determining how the work function evolves during the oxygen-lithium surface treatment cycles. Measurements were obtained by taking two sweeps of the BS1 sample surface with 1-second dwell times across a range of 19 eV to -0.5 eV. An iris aperture was also used to improve the resolution of the secondary electron peak, modelled as the sharp peak in the spectra of Figure 16.

3.4.3 Photoemission Electron Microscopy (PEEM)

PEEM is an imaging technique used alongside UPS that allows spatially resolved measurement of photoelectron emission from surfaces. In PEEM, photoelectrons emitted from the sample are accelerated by an electrostatic field and focused onto a detector to form an image of the emitting surface [58]. Because the intensity of emitted electrons depends on the local work function, PEEM images can reveal spatial variations in electron emission properties across the sample surface [59].

Energy-filtered (EF-) PEEM systems can provide even more detailed information. By selecting electrons within a narrow kinetic energy window, it is possible to map the local work function across the surface with high spatial resolution [58].

EF-PEEM has been widely used in studies of diamond electron emitters because it allows researchers to visualise variations in emission behaviour across heterogeneous surfaces after various functionalisation processes. Previous work, as seen in Figure 17, has shown that surface defects, grain boundaries and variations in surface termination can produce significant local variations in work function [24].

In this project, EF-PEEM was used to generate spatially resolved work function maps of the diamond samples before, during, and after surface functionalisation. A region representative of the overall surface was selected and consistently re-scanned following each O-Li functionalisation cycle to ensure direct comparison. Repetitive scans consisted of three sweeps over a 2.5 eV to 5.5 eV energy range and 40 μm FOV with 5-second dwell times at 12 kV. The iris aperture was used along with the He I ($h\nu = 21.2\ eV$) radiation source as for UPS.

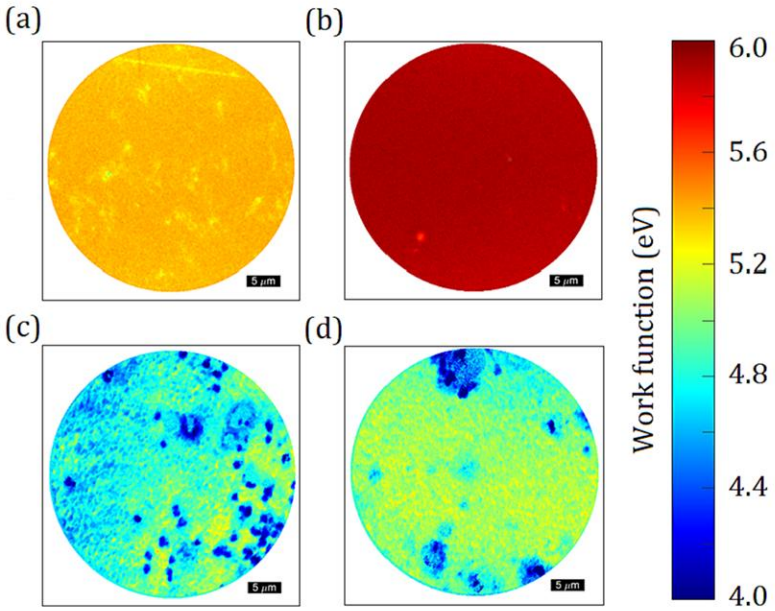

Figure 17: Spatially resolved EF-PEEM work function maps of oxygen-terminated diamond (100) surfaces prepared using different oxidation techniques: (a) O_2 plasma, (b) UV-ozone, (c) O_2 cracking, and (d) acid oxidation. Each pixel is a spectrum with an associated work function revealing differences in surface uniformity and electronic structure induced by each treatment. 37.5 μm FOV map. After [24].

3.4.4 Spot Profile Analysis Low Energy Electron Diffraction (SPA-LEED)

SPA-LEED provides reciprocal-space information on surface crystallography by analysing the diffraction pattern produced when a low-energy electron beam scatters elastically from the periodic arrangement of the topmost atomic layers of the surface [42, 60]. Unlike conventional LEED, SPA-LEED records not just the location, but also the shape profile of diffraction spots, making it extremely sensitive to small variations in surface order [60].

SPA-LEED patterns demonstrate that while both hydrogen- and oxygen-treated diamond surfaces retain long-range crystallographic order, the surface chemistry significantly influences the observed reciprocal-space features. The hydrogen-terminated surface in Figure 18(c) exhibits sharp, symmetric diffraction spots consistent with a well-ordered, minimally reconstructed (1×1) structure. Figure 18(a, b) by contrast, exhibits oxygen-treated surfaces that display variations in spot intensity and shape, including elongation and anisotropy, indicative of surface reconstruction and increased structural complexity arising from C-O bonding.

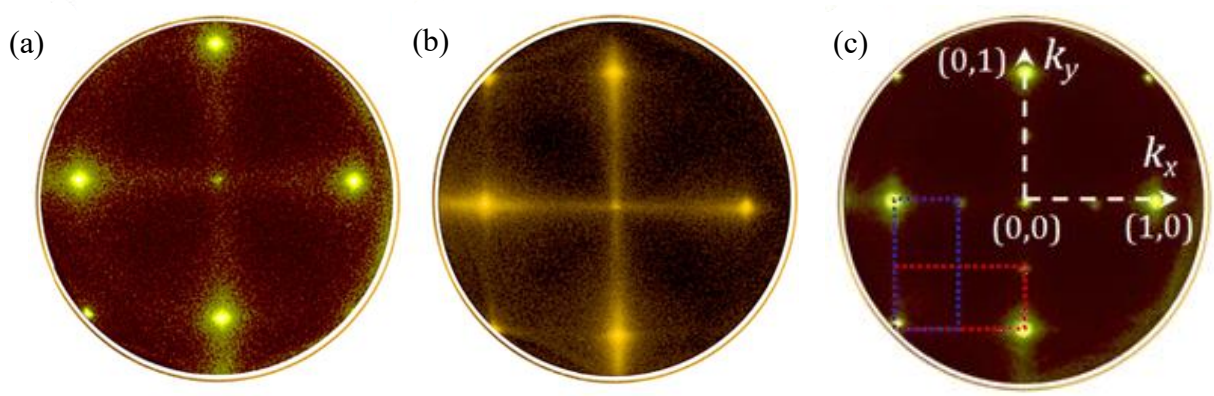

Figure 18: Exemplar SPA-LEED patterns of diamond (100) surfaces after oxygen termination via (a) O_2 plasma and (b) UV-ozone treatment, recorded at 130 eV. After [24]. (c) Hydrogen-terminated (100) bare surface, from [11]. The symmetry and sharpness of the diffraction spots reflect the degree of surface order and reconstruction, enabling assessment of the structural quality and uniformity of the surface.

In the context of this project, being able to observe SPA-LEED is essential for assessing whether the diamond surfaces exhibit the atomically smooth, well-ordered reconstructions needed for reliable work function measurements following annealing and functionalisation treatments. Measurements were taken over a 200x200 point rage at 30 ms each and carried out at ~146 eV and ~94 eV to find the (1, 1) and (0, 0), and (1, 0) diffraction spots, respectively.

3.5 Data Fitting and Models

3.5.1 CasaXPS

At the outset of the XPS analysis, all spectra were processed and fitted using the following methodology. A Shirley-type background, arising from inelastic scattering of photoelectrons, was first modelled and subtracted from each spectrum to isolate the true photoemission signal. High-resolution C 1s, O 1s and Li 1s spectra were then fitted in CasaXPS using asymmetric Voigt (GL) line shapes, which account for both instrumental broadening (Gaussian contribution) and intrinsic lifetime effects (Lorentzian contribution). For each surface treatment, a fitting model was constructed based on expected chemical states and literature binding energy separations, particularly those associated with molecular oxygen and oxygen-lithium functionalisation seen in Table 1. The dominant peak in each region was first assigned to the most probable chemical state (e.g. sp^3 C-C (B) in C 1s), and additional component peaks were introduced with constrained binding energy offsets derived from reported values. Model optimisation was performed by minimising the residual between the fitted envelope and experimental data, while maintaining physical consistency: identical chemical states were constrained to share the same line shape, and full width at half maximum (FWHM) values were kept constant within each spectral region unless justified by distinct chemical environments. Relative component contributions were subsequently quantified using peak areas, adjusted by appropriate sensitivity factors, allowing direct comparison of chemical composition across surface treatments.

Core Level	Treatment	Surface Component	MolO SCD (100) BE (eV)	MolO Rel. (%)
C 1s	Pre-lithiation	sp^3 C–C (B)	284.43	86.4
		sp^3 C–C (S)	285.03	10.3
		C–O	285.83	2.2
		C=O	287.23	1.1
O 1s	Pre-lithiation	C–O–C	533.84	2.9
		C–OH	532.31	73.3
		C=O	531.63	23.9
	Lithiated	C–O–C	533.3	11
		C–OH	532.45	28.6
		C=O	531.6	19.9
		C–O–Li	530.52	13.6
		Li_2O	529.35	27
Li 1s	Lithiated	Li^0 (Li–Li)	54.5	32.1
		C–O–Li (Li_2O)	55.79	67.9

Table 1: Chemical binding energy values, dependent on near-surface electrostatics [61], reported to one decimal place, and their relative percentages taken from a (100) SCD surface at different stages of lithiation using molecular oxygen exposure. Obtained from C 1s, O 1s and Li 1s core level XPS spectra. Adapted from [20].

3.5.2 Python Code for UPS Fitting

The UPS spectra were processed and plotted using a Python script that imports the experimental binding energy-intensity data from an Excel file and applies a Savitzky-Golay filter to smooth noise while preserving spectral features. The valence band maximum (VBM) and SECO were determined by identifying regions of maximum gradient and performing linear fits to these edges, with the intercepts used to extract their respective energies.

3.5.3 Work Function Mapping in MATLAB

Finally, a MATLAB code was used to construct work function maps by analysing a stack of energy-resolved EF-PEEM images. It extracts the electron intensities over an energy scale from the collected data along with FOV adjustments. For each pixel, the code computes the intensity gradient across energy and identifies the point of maximum gradient, which corresponds to the local SECO. A linear extrapolation of this edge is then used to determine the cutoff energy pixel-by-pixel, from which the local work function is calculated.

4. Results and Discussion

4.1 Comparison of Hydrogen-Terminated Surfaces BS1 & BS3

4.1.1 Chemical Composition

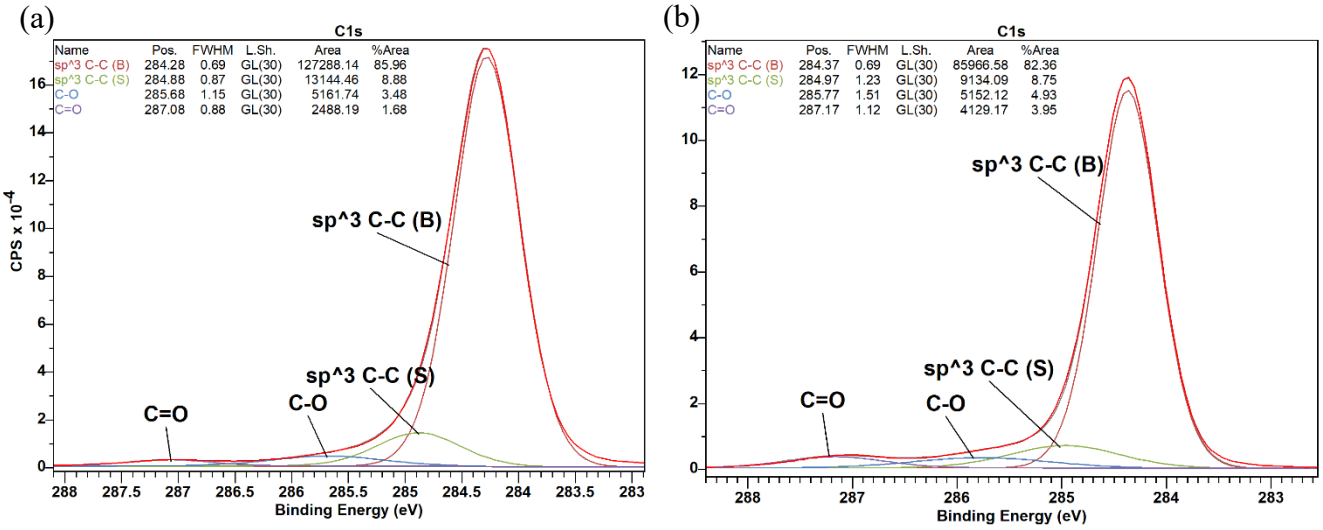

Figure 19: Fitted core-level XPS.1 spectra of the C 1s peaks for the (110) hydrogen-terminated (a) BS1 and (b) BS3 BDD samples. Original spectra of the collected XPS data shown in bright red, with fitted chemical components colour coded by the key shown in figure. sp^3 C-C (B) and sp^3 C-C (S) represent 'Bulk' and 'Surface' C-C bonds, respectively.

The C 1s spectra in Figure 19(a, b) are consistent with predominantly sp^3-bonded carbon in the near-surface region of the (110) hydrogen-terminated BDD, with no strong evidence for a distinct sp^2 (graphitic) contribution within the fitting uncertainty. The dominant sp^3 C-C (B) component, with a binding energy of 284.28 eV for BS1, taken from Figure 19(a), and 284.37 eV for BS3, taken from Figure 19(b), both have greater than 80% contribution within commonly reported ranges for diamond-like sp^3 carbon as shown in Table 1. The higher binding energy sp^3 C-C (S) component, displaced by ~+0.60 eV with only ~8.8% contribution, is consistent with a near-surface core-level shift or carbon bonded to adsorbates. On (110) diamond surfaces, a shifted sp^3 C-C (S) component of ~+0.8 eV has been reported [29] on plasma-hydrogenated samples and attributed to co-adsorbed hydrocarbons rather than hydrogen termination alone, indicating that such shifts can arise from a combination of surface termination state and adventitious carbon. The smaller shift observed here is therefore consistent with comparatively limited hydrocarbon adsorption from the preparation.

One possible explanation for the larger sp^3 C-C contribution observed for BS1 in Figure 19(a) relative to BS3 in Figure19(b) suggests that a greater proportion of carbon atoms remain in a bulk-like diamond environment, whereas BS3 has a larger fraction of carbon distributed across surface states away from the main sp^3 peak. On the other hand, the large difference in area between samples could also arise from experimental factors such as surface alignment or variations in electronic properties which affect emission yield, resulting in differences in photoelectron signal intensity.

Another principal difference between BS1 and BS3 is the fitted fraction of oxygen-shifted carbon components within the C 1s envelope. BS3 exhibits a larger oxygen-shifted contribution of 8.88% than BS1's 5.16%, driven mainly by an increased ketone component C=O. Ether C-O-C bonding is expected to dominate over ketone formation due to its lower binding energy, making it energetically more favourable and more readily stabilised on the diamond surface. These higher-binding-energy components fall within typical chemical-shift ranges for C-O and C=O bonds on diamond surfaces, consistent with limited surface oxidation [62]. However, because the C 1s signal exhibits such a relatively large sp^3 C-C (B) contribution in diamond, these fitted fractions should be interpreted as comparative indicators of surface functionalisation rather than direct measures of oxygen coverage [17]. Overall, the low intensity of oxygen-shifted C 1s components support the conclusion that both surfaces remain predominantly hydrogen-terminated, with minor oxygen adsorbates likely arising from ambient exposure and residual vacuum contamination [17].

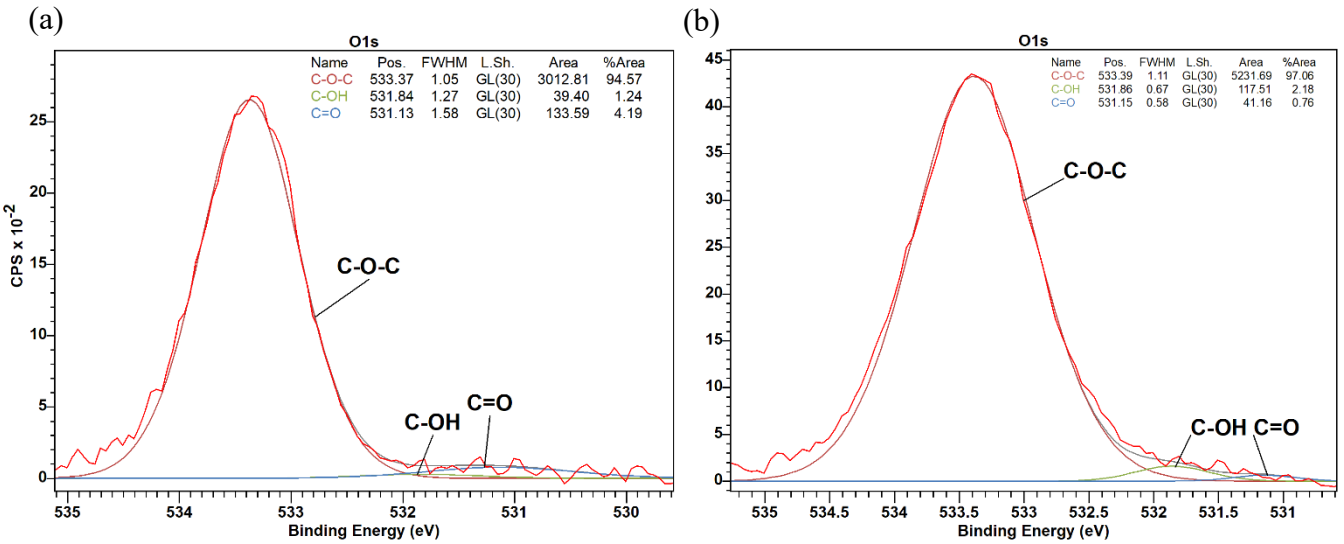

Figure 20: Fitted core-level XPS.1 spectra of the O 1s peaks for the (110) hydrogen-terminated (a) BS1 and (b) BS3 BDD samples. Original spectra of the collected XPS data shown in bright red, with fitted chemical components colour coded by the key shown in figure. sp^3 C-C (B) and sp^3 C-C (S) represent 'Bulk' and 'Surface' C-C bonds, respectively.

The O 1s spectra for BS1 and BS3, presented in Figure 20, again indicate low overall oxygen content due to the low-intensity peaks, reflective of a predominantly hydrogen-terminated surface. The dominant O 1s component at ~533.4 eV with greater than 90% contribution for both BS1 and BS3 is consistent with C-O-C bond binding energies [20] and given the small oxygen-shifted fraction in the C 1s spectra, this component is more accurately attributed to weakly bound or adventitious oxygen species [17]. Minor components at ~531 eV are consistent with stronger oxidisation, but their small relative intensity shows they are not the dominant surface species.

The larger C 1s peak area observed for BS1 in Figure 19(a) compared to BS3 in Figure 19(b) is consistent with its significantly lower O 1s area in Figure 20(a). This reduced surface oxidation suggests a better quality of hydrogen-termination, whereas the increased BS3 O 1s signal in Figure 20(b) corresponds to a greater fraction of adventitious oxygen adsorption. Consequently, BS1 represents a more successfully hydrogen-terminated surface, exhibiting a purer sp^3 C-C bonded composition.

4.1.2 Work Function Comparison

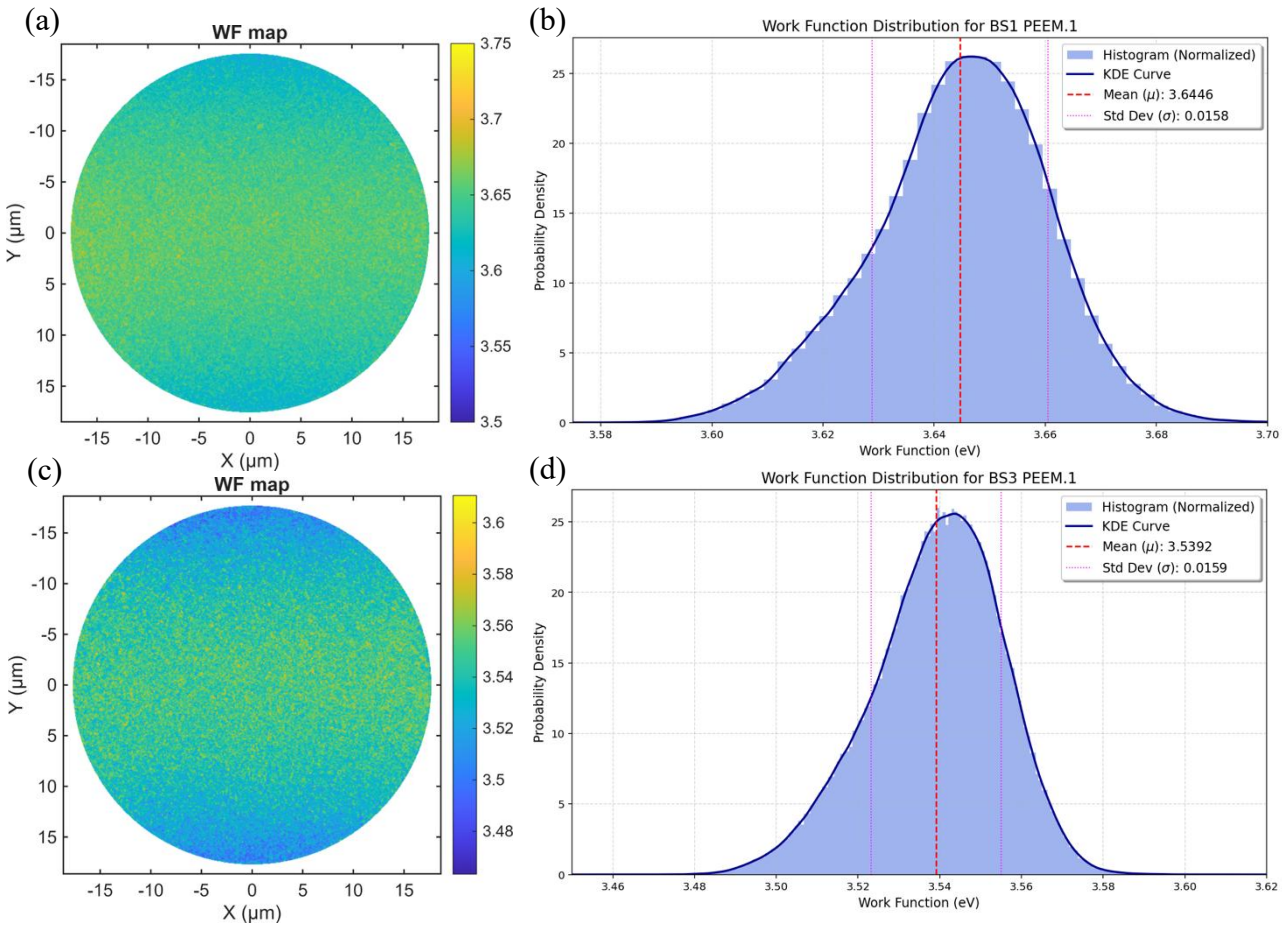

Figure 21: Work function (WF) maps and their corresponding probability distributions for the (110) hydrogen-terminated (a, b) BS1 and (c, d) BS3 BDD samples obtained from EF-PEEM.1 experimentation. The colour scale shown to the right of the WF maps represents the work function range in eV. Mean work function values and their respective errors have been calculated from the plotted distributions.

The derived EF-PEEM work functions presented in Figure 21(a, b) of 3.64 ± 0.02 eV for BS1 and in Figure 21(c, d) of 3.54 ± 0.02 eV for BS3 are both low with respect to hydrogen-terminated diamond (110), where literature values of a 3.5 eV - 3.9 eV range are typically reported for clean surfaces [12, 63, 64]. The narrow confidence on the fitted mean of ± 0.02 eV, seen in both Figure 21(b, d), reflects the statistical precision of the histogram analysis. The slightly lower work function observed for BS3, despite its higher oxygen-related XPS contribution, suggests that its surface electronic structure is influenced not only by oxygen contamination but also by local variations in hydrogen coverage, band bending, or surface dipole formation.

In contrast, BS1, which is chemically cleaner in XPS, exhibits a marginally higher work function, consistent with a more uniform but potentially less dipole-enhanced surface. This behaviour aligns with previous Bristol results, where hydrogen-terminated (110) surfaces show a work function of 4.0 eV and are highly sensitive to subtle changes in surface chemistry and preparation conditions [25]. In Bristol NanoESCA diamond studies, EF-PEEM mapping is performed via threshold image series with an energy resolution of order 0.15 eV, and the extracted work function values are commonly corrected for the Schottky barrier lowering, induced by the high extractor field: $\Delta\Phi \approx 98$ meV for 12 kV across ~1.8 mm [10]. This leaves an overall work function uncertainty of

order ± 0.15 eV [10]. Accordingly, the ≈ 0.10 eV difference between BS1 and BS3 is best treated as a modest trend rather than a definitive quantitative separation in absolute work function.

Figure 21(a, c) also present work function maps that reflect smooth and spatially uniform surfaces with only minor fluctuations, indicating a chemically homogeneous surface with minimal contamination, consistent with a well-prepared and largely clean hydrogen-terminated diamond surface. The apparent decrease in work function at the top and bottom of the map is most likely an edge effect rather than chemical variation. Near the edges of the FOV, reduced signal intensity and variations in extraction field uniformity within the EF-PEEM instrument can lead to slight shifts in the measured SECO, artificially lowering the extracted work function.

4.1.3 NEA Calculation

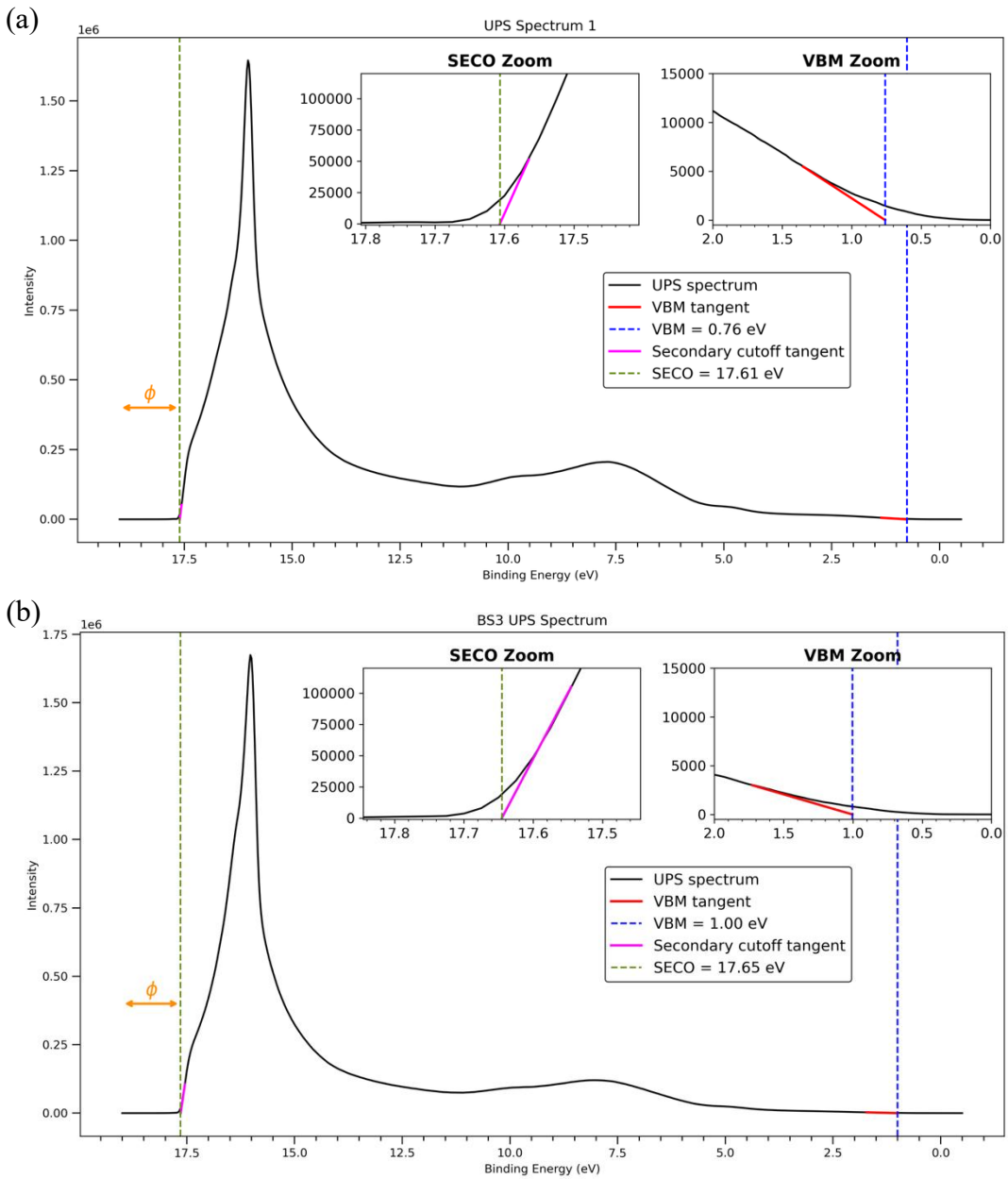

Figure 22: UPS.1 spectra for the (110) hydrogen-terminated (a) BS1 and (b) BS3 BDD samples, showing the secondary electron peak, presented over the full photoelectron binding energy range measured. Zoomed in plots show the fit of the extrapolated SECO and VBM tangents, with their corresponding values indicated in the key.

Using the UPS spectra in Figure 22(a, b), work functions of 3.59 eV for BS1 and 3.55 eV for BS3 were obtained via Equation (6), using the extrapolated VBM and SECO tangents. E_F has also been normalised to 0 eV. While these values are consistent with hydrogen-terminated diamond, the derived EF-PEEM work functions (3.64 ± 0.02 eV for BS1 and 3.54 ± 0.02 eV for BS3) are taken as more reliable due to the superior spatial resolution and reduced sensitivity to background fitting and SECO extrapolation. Using these PEEM values, the corresponding NEA values were calculated using Equation (7) and Equation (8) as -1.07 ± 0.02 eV for BS1 and -0.93 ± 0.02 eV for BS3. These values are in good agreement with reported literature values of approximately -1.0 eV for hydrogen-terminated diamond (110) surfaces [25]. The slightly more negative NEA observed for BS1 is consistent with its lower oxygen content identified in XPS, as oxygen-related surface states are known to increase the work function and suppress NEA by modifying the surface dipole. This trend is supported by prior studies, which show that even small levels of oxygen adsorption can measurably reduce NEA magnitude and increase work function on diamond surfaces [20]. Overall, the initial phase of the project was successful in creating smooth surfaces with low work function bases upon which subsequent surface functionalisation can commence.

4.2 Surface Reconstruction SPA-LEED Analysis

(a) (b)

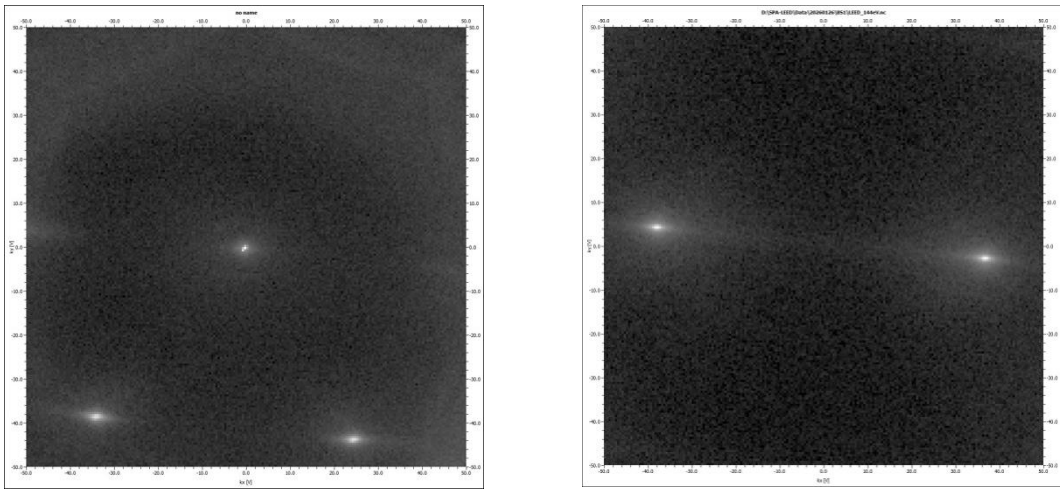

Figure 23: Reciprocal-space SPA-LEED.1 patterns obtained at a beam energy of (a) 96 eV to show the (0, 0) and (1, 1) diffraction spots, and (b) 144 eV to show the (1, 0) diffraction spots of the (110) hydrogen-terminated BS1 BDD sample.

The observation of clear SPA-LEED diffraction spots in Figure 23(a, b) from the BS1 hydrogen-terminated (110) surface is itself strong evidence that the surface is both atomically smooth over the coherence length of the electron beam and well-ordered in reconstruction, since disorder, or heavy contamination would broaden or suppress the diffraction pattern into background intensity. The combinations of diffraction spots being resolved under different beam strengths reflects the energy dependence of SPA-LEED spot intensity. Different beam

energies satisfy different scattering conditions and enhance different reciprocal-lattice points, so imaging at more than one energy is necessary to optimise visibility of specific diffraction features and confirm the periodicity of the surface.

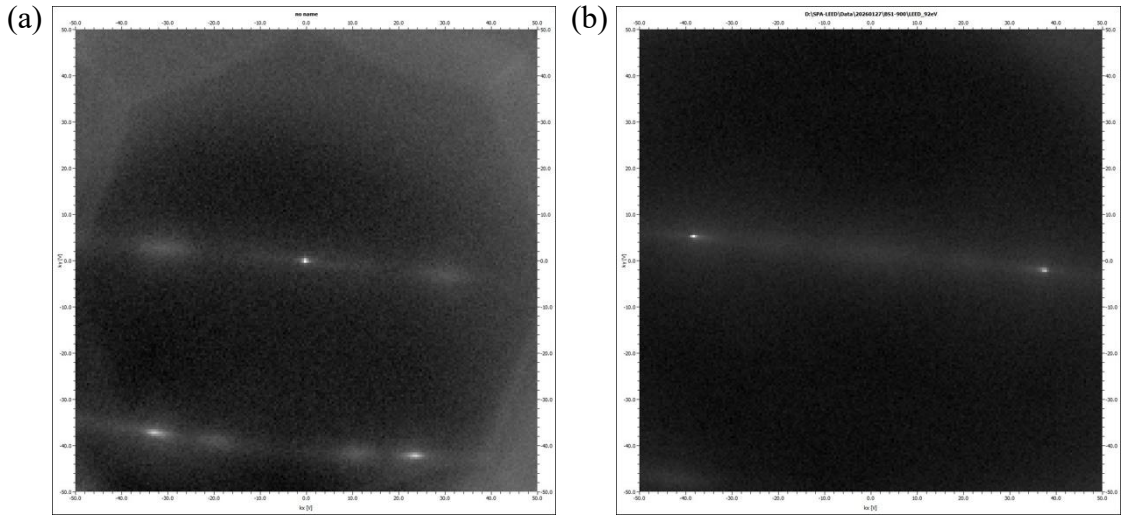

Figure 24: Reciprocal-space SPA-LEED.2 patterns obtained at a beam energy of (a) 92 eV to show the (0, 0) and (1, 1) diffraction spots, and (b) 148 eV to show the (1, 0) diffraction spots of the (110) BS1 BDD sample after a 900 °C anneal, where all hydrogen termination is assumed to be removed.

The sample underwent a 900 °C anneal for the duration of 1 hour to remove surface hydrogen termination. The anneal successfully reset the surface chemistry by removing almost all chemically terminated bonds, as seen by the significantly small area of the O 1s peak measured in Figure 1 of the appendix. This is further confirmed by the large increase in area of the corresponding C 1s spectra covered in sp^3 C-C (S) bonds, depicted in Figure 2 of the appendix. Following the anneal, Figure 24(a, b) shows a sharpening of diffraction spots and reduced background, indicating an improved surface order as shown in ab initio studies [21, 65]. This is consistent with the removal of adsorbates and enhanced surface reconstruction [24], producing a smoother and more uniformly ordered (110) surface. Importantly, the emergence of faint half-order spots suggests the development of a more ordered reconstructed surface with increased periodicity, consistent with reports that annealing induces distinct LEED reconstructions such as (2×1) ordering following hydrogen desorption [66]. This interpretation is supported by recent reports, where a 900 °C hydrogen desorption anneal reduced oxygen contamination from 1.8 atomic % to 0.3 atomic % and broadened the C 1s peak by about 0.3 eV, showing that the anneal substantially altered the near-surface chemical state while improving cleanliness [17].

4.3 Testing the Efficacy of the NEG

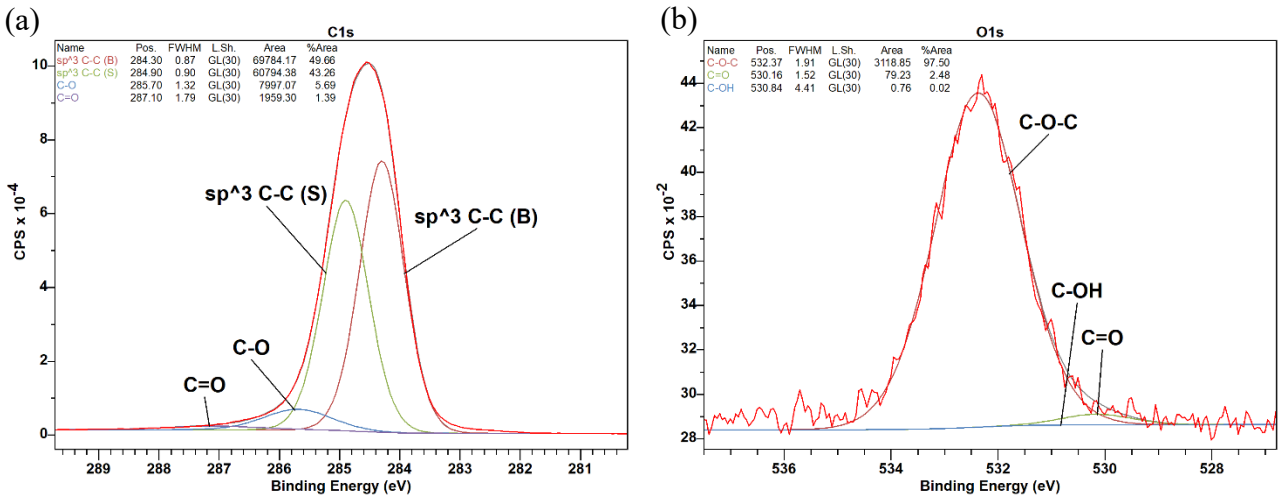

Figure 25: Fitted core-level XPS.3 spectra of the (a) C 1s and (b) O 1s peaks for the (110) BDD sample after undergoing molecular oxygen treatment at a pressure of 1×10^{-2} mbar for 5 minutes. Original spectra of the collected XPS data shown in bright red, with fitted chemical components colour coded by the key shown in figure. sp^3 C-C (B) and sp^3 C-C (S) represent 'Bulk' and 'Surface' C-C bonds, respectively.

A NEG was introduced following the collection of the UPS.1 data. Post both SPA-LEED analyses and the 900 °C anneal, the BS1 (110) diamond surface underwent a singular treatment of molecular oxygen exposure at 1×10^{-2} mbar for 5 minutes. The large sp^3 C-C (S) component area seen in Figure 25(a) can be interpreted as evidence of a partially oxidised, chemically heterogeneous surface, as molecular oxygen is insufficiently energetic to bind to all available surface sites, retaining a large the number of the surface sp^3 C-C bonds measured post-anneal.

The percentage of oxygen coverage was subsequently calculated through analysis of the fitted O 1s and C 1s XPS core-level spectra. The relative atomic concentration of oxygen was determined using the method implemented in [20]:

$$O\% = \frac{\frac{A(O\ 1s)}{RSF(O\ 1s)}}{\left[\frac{A(O\ 1s)}{RSF(O\ 1s)} + \frac{A(C\ 1s)}{RSF(C\ 1s)}\right]} \times 100\% \tag{9}$$

Where A represents the total fitted peak area for each core level and the relative sensitivity factor (RFS) ratio for O 1s to C 1s is taken as 2.93:1. This approach assumes a uniform distribution of oxygen within the XPS probing depth, whilst recognising that signal contributions from underlying bulk sp^3 C-C bonds lead to an underestimation of the true surface coverage.

Applying this calculation to the spectra shown in Figure 25(a, b), where the O 1s peak in Figure 26(b) is dominated by a C-O-C component at ~532.37 eV with significantly smaller contributions from C=O and C-OH species, yields an oxygen coverage of 0.77%. Recent literature suggests that a relative atomic concentration of ~7.2% represents full oxygen coverage on a (100) diamond substrate [20, 24], corresponding to an effective surface coverage of ~10% in these findings.

This value is significantly lower than a previously reported oxygen coverage of approximately ~2% for a molecular oxygen-treated (110) diamond sample under comparable exposure conditions (1×10^{-2} mbar for 10 minutes) [17, 25]. These reports of higher oxygen coverage indicate a more effective oxidation of the diamond surface, likely corresponding to a greater proportion of surface carbon atoms participating in ether C-O-C and ketone C=O bonding configurations.

As highlighted in [20], molecular oxygen exposure alone is often insufficient to fully replace hydrogen termination due to the relatively low kinetic energy of oxygen, meaning that residual hydrogen can persist or re-adsorb onto the surface. The reduced oxygen coverage in this project does not align with the expected results of implementing of a NEG. The NEG was predicted to significantly reduce the residual hydrogen within the NanoESCA chamber and consequently increase the number of unsatisfied dangling bonds available for oxygen adsorption. Based on this evidence, one conclusion is that the NEG has been ineffective.

However, oxygen coverage is arguably not the most reliable method of testing the efficiency of the NEG and instead the percentage of observed hydroxyl (C-OH) bonds should be taken as a likely indicator of the level of remaining residual hydrogen. An alternative conclusion claims that the NEG has still been successful in suppressing hydrogen re-adsorption, thereby limiting the availability of reactive sites formed via hydrogen displacement processes. The trace amount of C-OH visible in Figure 25(b) instead indicates that the surface is less contaminated by residual hydrogen and more representative of a controlled adsorption process governed purely by molecular oxygen interaction with a clean diamond surface.

A lower but more well-defined oxygen coverage may promote greater control over O-Li bonding configurations, reducing the formation of competing species associated with hydrogen contamination. However, it also suggests that achieving high oxygen coverage may require either increased exposure time or lower oxygen pressures, indicated by the saturated 1×10^{-3} mbar molecular oxygen exposure performed by [25].

4.4 Oxygen-Lithium Cycling

4.4.1 O 1 s Surface Composition

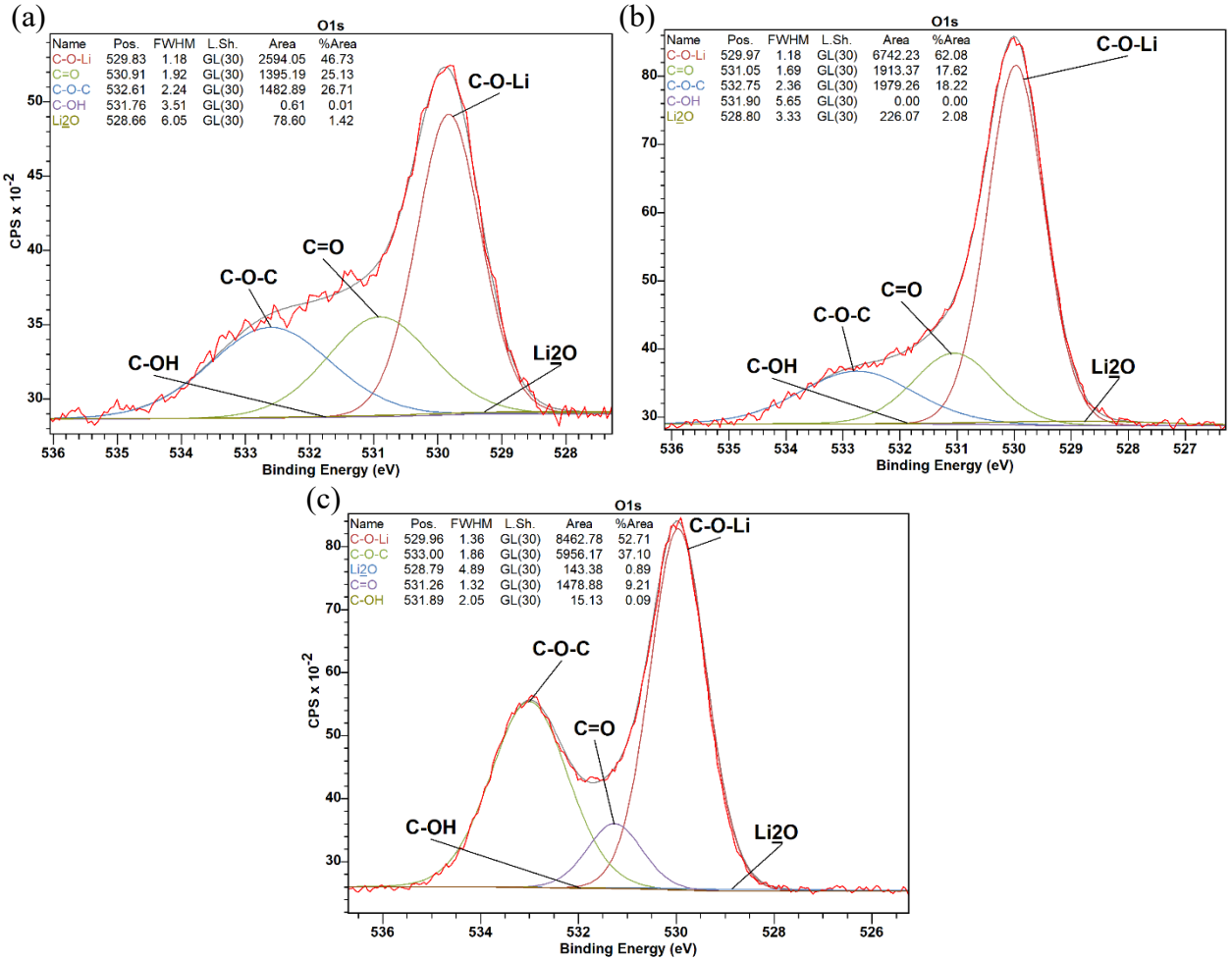

Figure 26: Fitted core-level XPS spectra of the of the O 1s peaks following the (a) 1st (XPS.4), (b) 2nd (XPS.5), and (c) 3rd (XPS.6) cycles of molecular O-Li treatment for the (110) hydrogen-terminated BS1 BDD sample. Original spectra of the collected XPS data shown in bright red, with fitted chemical components colour coded by the key shown in figure. sp^3 C-C (B) and sp^3 C-C (S) represent 'Bulk' and 'Surface' C-C bonds, respectively.

The progression of the O 1s spectra from XPS 4 to XPS 6 provides clear evidence that oxygen-lithium cycling acts as an iterative surface-engineering process, rather than a simple accumulation of lithium. Figure 26(a) shows that after the first cycle (XPS 4), the appearance of a substantial C-O-Li component of ~47% alongside residual C-O-C and C=O indicates that lithium has already reacted with oxygen-terminated sites to form dipole-active O-Li bonds, while the near absence of C-OH throughout the treatment cycles supports the argument for the success of the NEG, as previously discussed. This behaviour is consistent with the mechanism reported by [20], where lithium preferentially reacts with oxygen-containing species to form C-O-Li, shifting the O 1s intensity to lower binding energy. The second cycle shown in Figure 26(b) (XPS 5) enhances this process, increasing the C-O-Li contribution to ~62% and almost tripling its area, demonstrating more extensive lithium incorporation and a move toward a more homogeneous dipole-forming surface. Notably, this level of C-O-Li bonding already exceeds that reported for molecular oxygen-treated diamond (100) after initial lithiation of 13.6% published in [20], suggesting more efficient incorporation on the (110) surface under the present conditions.

The third cycle (XPS 6), presented in Figure 26(c), reveals that the process continues to yield a steady increase in the area of C-O-Li, however not as large a difference as between XPS.4 and XPS.5, indicating that the surface has started to stabilise. However, its contribution decreases to ~53% while C-O-C increases significantly to a ~37% portion and tripling its area. This exhibits a similar trend to C-O-Li in XPS.5, most plausibly attributed to surface reorganisation after saturation of the more favourable C-O-Li binding sites. Once lithium uptake becomes limited, additional oxygen exposure is expected to redistribute the oxygen over-layer into more stable non-lithiated configurations, particularly bridging ether species, rather than producing a further substantial increase in C-O-Li. This behaviour aligns with observations in the Bristol (110) studies [17, 25], which report that successive O-Li cycles lead to progressive changes in the O 1s spectrum, with low binding energy O-Li features increasing initially before the surface chemistry stabilises and saturates after further treatments. These reports further show that improvements in electronic properties, such as reduced work function and enhanced NEA, continue even when the chemical composition evolves in a non-linear way, highlighting that the final surface state reflects an optimised balance of bonding configurations rather than maximum lithium coverage alone [17]. Across all three cycles in the present work, the consistently minimal Li_2O contribution being < 2% is particularly important, as it confirms that lithium is not forming a thick oxide over-layer, as seen in some (100) studies where Li_2O can reach 27% [20], but instead remains primarily incorporated into interfacial C-O-Li bonds that directly contribute to surface dipole formation.

4.4.2 Li 1s Surface Composition

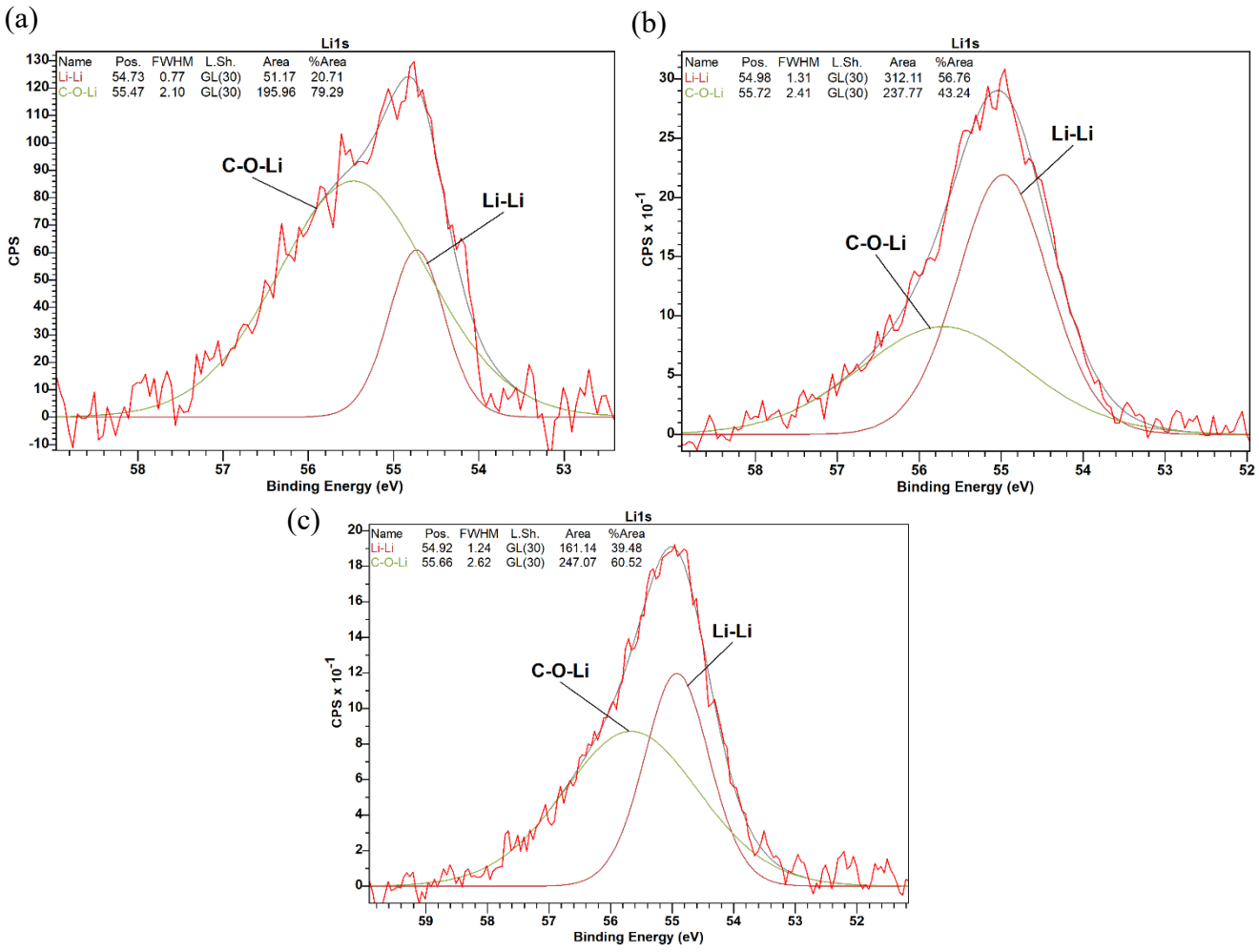

Figure 27: Fitted core-level XPS spectra of the of the Li 1s peaks following the (a) 1st (XPS.4), (b) 2nd (XPS.5), and (c) 3rd (XPS.6) cycles of molecular O-Li treatment for the (110) hydrogen-terminated BS1 BDD sample. Original spectra of the collected XPS data shown in bright red, with fitted chemical components colour coded by the key shown in figure. sp^3 C-C (B) and sp^3 C-C (S) represent 'Bulk' and 'Surface' C-C bonds, respectively.

Figure 27(a) shows that after the first cycle (XPS.4), the spectrum is dominated by an ~80% contribution of the C-O-Li component at a binding energy of ~55.5 eV, with a smaller Li-Li contribution of ~20% at a binding energy of ~54.7 eV. This indicates that lithium is initially incorporated efficiently into oxygen-terminated sites. This behaviour again agrees with literature [20], where lithium preferentially forms ionic O-Li bonds on oxygenated diamond due to strong charge transfer to electronegative oxygen, stabilising a dipole-active surface.

Following the second cycle (XPS.5), presented in Figure 27(b), the surface chemistry shifts, metallic Li-Li dominating over 50% of measured bonds and its area multiplying six-fold, compared to the relatively slight area increase in C-O-Li bonding. This increase implies that a large portion of available oxygen-bonding sites have become saturated after the first cycle, so additional lithium deposition cannot be fully accommodated as O-Li bonding and instead accumulates as metallic lithium. Such behaviour has been observed in both Bristol (110) studies [33, 40] and molecular oxygen-treated (100) surfaces [17], where excess lithium forms clusters or weakly bound metallic states once oxygen coverage becomes limiting.

The Li 1s spectrum shown in Figure 27(c) for Li 1s XPS 6, recorded after the third and final oxygen-lithium cycle, shows the trend partially reversing: the C-O-Li component regains the majority contribution of ~60%, while its area remains constant. These finding suggest that further oxygen-lithium exposure does not lead to a significant increase of C-O-Li bonding, confirming the saturation seen in the O 1s peaks. The Li-Li area halves, reducing its contribution to ~40%, suggesting that the anneal has successfully removed a large portion of the previously accumulated, and weakly bonded metallic lithium. This demonstrates that the third cycle has driven the system toward a more stable configuration.

This trend is also consistent with the Bristol (110) research [17, 25], which found that successive oxygen-lithium cycles gradually increased the importance of ionic O-Li bonding relative to Li-Li, and linked this evolution to the eventual reduction in work function and enhancement of NEA. Their results emphasised that the key indicator of successful surface functionalisation is not total lithium uptake, but the balance shifting from metallic Li aggregates toward chemically bonded O-Li species. In this context, XPS 6 indicates that the third cycle is the point at which the surface chemistry becomes optimised without over saturating the surface with metallic lithium.

4.4.3 Work Function and NEA

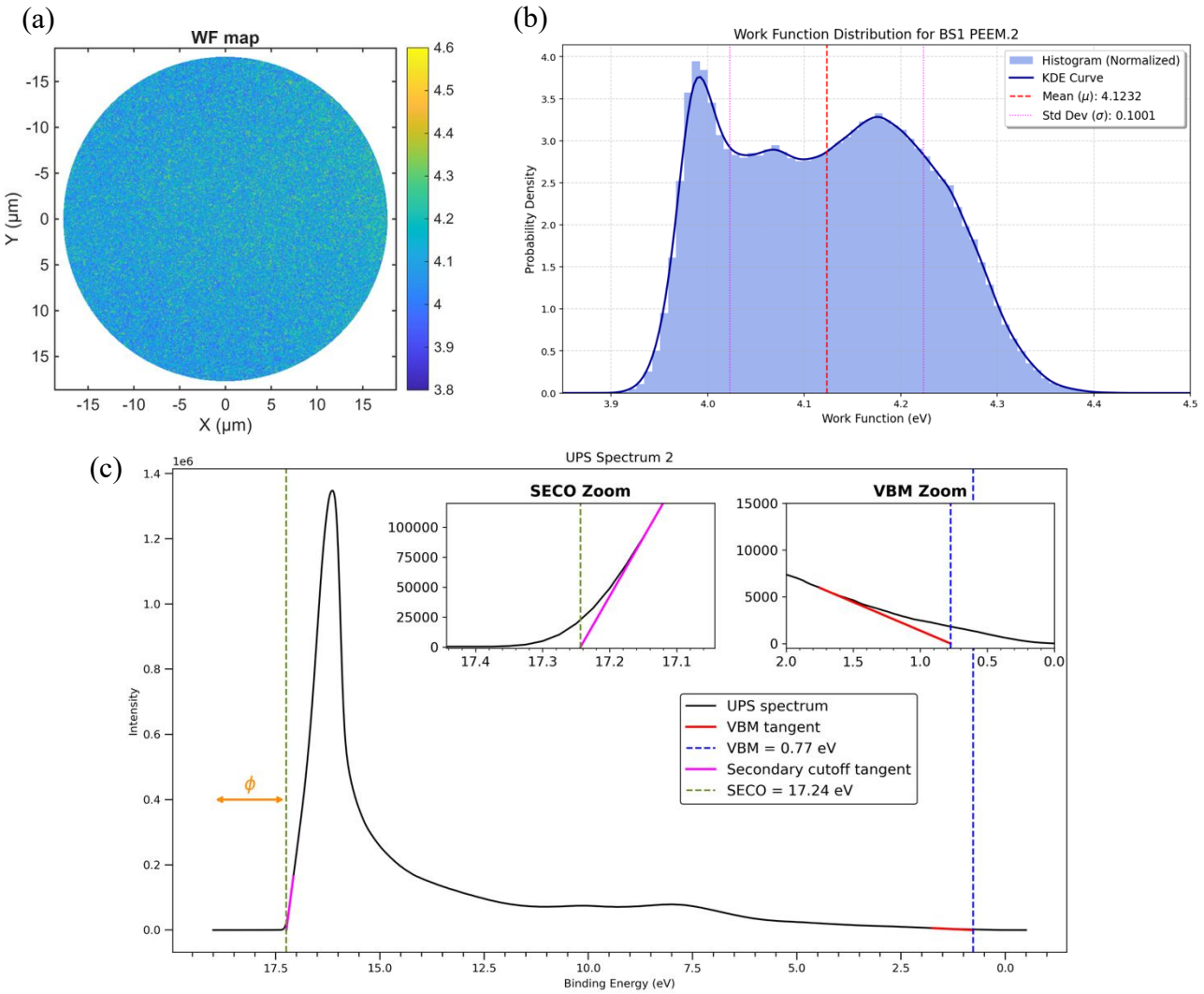

Figure 28: (a) Work function (WF) map, (b) its corresponding probability distribution obtained from EF-PEEM.2 data, and (c) UPS.2 spectra for the (110) hydrogen-terminated BS1 BDD sample after the 1st cycle of molecular O-Li treatment.

After the first oxygen-lithium cycle, EF-PEEM.2 data in Figure 28(a, b) measured a work function of 4.12 ± 0.10 eV, reflecting a surface dominated by oxygen termination, despite the emergence of O-Li bonding. The XPS spectrum in Figure 26(a) confirms that while C-O-Li species have formed, a significant fraction of oxygen bonds such as C-O-C and C=O with higher binding energies remain, which are known to increase the work function and shift the surface toward PEA. The resulting NEA of -0.58 ± 0.10 eV, calculated from Figure 29(c), therefore represents only a partial recovery of NEA, indicating that lithium incorporation has begun to counteract oxygen-induced dipoles, but has not yet fully restructured the surface into the optimised C-O-Li configuration. This intermediate behaviour is consistent with both Bristol research [17, 20, 25], where early-stage lithiation produces modest NEA that strengthens only after further cycling and increased O-Li bonding.

Although the probability density distribution of the EF-PEEM.2 data in Figure 28(b) does not have an ideal Gaussian distribution, leading to an increase in uncertainty of the work function value, crucially, the Figure

28(a) EF-PEEM.2 work function map remains highly uniform, demonstrating that the first cycle produces a chemically mixed but electronically homogeneous surface.

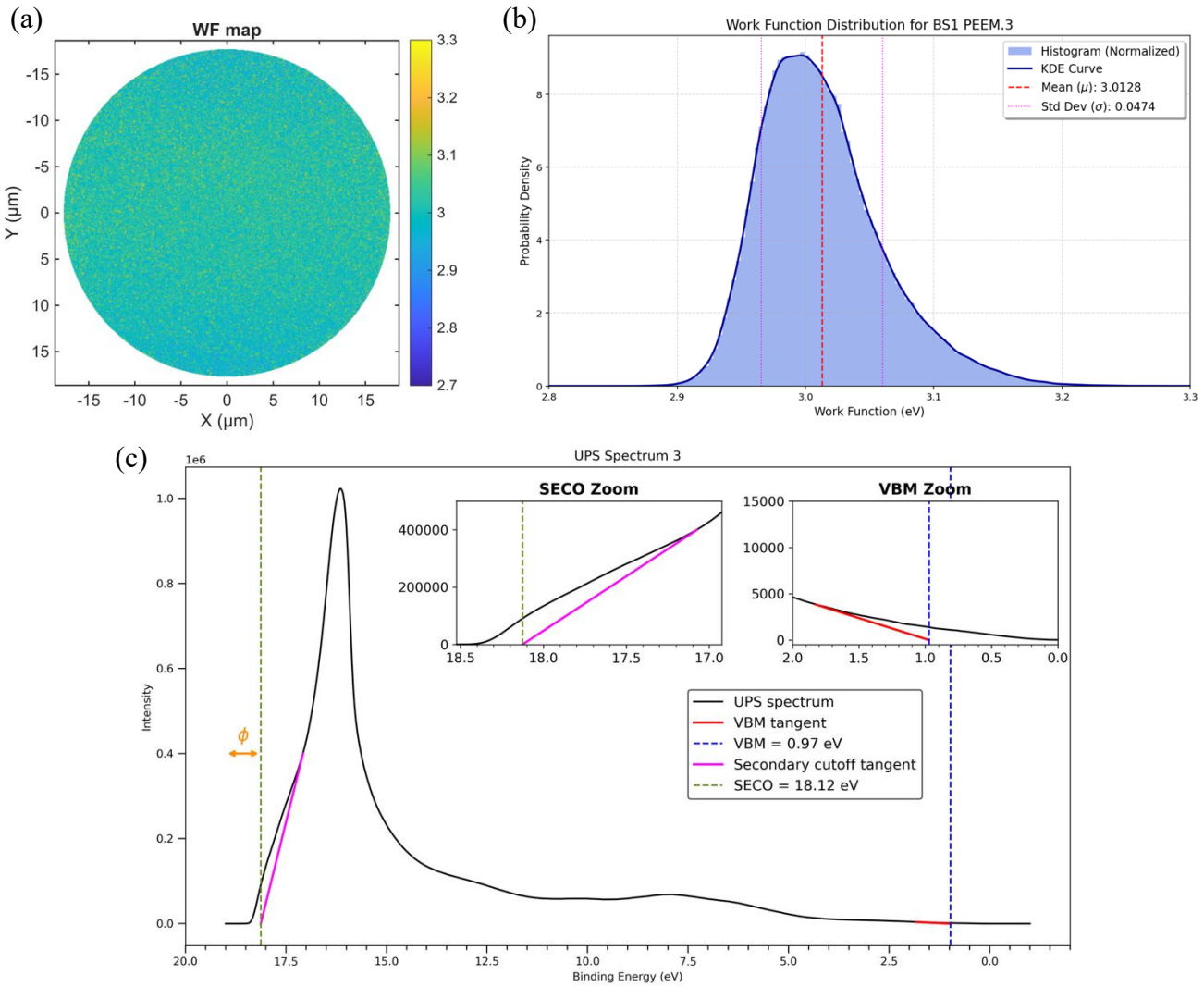

Figure 29: (a) Work function (WF) map, (b) its corresponding probability distribution obtained from EF-PEEM.3 data, and (c) UPS.3 spectra for the (110) hydrogen-terminated BS1 BDD sample after the 3rd cycle of molecular O-Li treatment.

After the third and final oxygen-lithium treatment cycle, the surface exhibits a fully optimised electronic structure consistent with a well-developed C-O-Li termination. The Figure 29(a, b) EF-PEEM.3 measurements yield a work function of 3.01 ± 0.05eV, representing a substantial reduction from the higher values observed after the initial cycle, and confirming that repeated cycling has effectively reversed the work-function increase introduced by oxygen termination. When combined with the UPS.3-derived valence band maximum, shown in Figure 29(c), this corresponds to an NEA of -1.49 ± 0.05 eV, indicating to a strongly electron-emissive surface. This magnitude of NEA is significant, as it demonstrates that lithium incorporation has progressed sufficiently to dominate the surface dipole, lowering the vacuum level below the conduction band minimum and establishing conditions favourable for efficient electron emission.

Importantly, the EF-PEEM.3 work function map remains highly uniform, with a narrow statistical distribution, indicating that the reduction in work function is achieved consistently across the surface rather than being localised to discrete regions. This reflects a high degree of homogeneity in the final surface chemistry, suggesting that the repeated oxygen-lithium cycling process has not only lowered the average work function but has also produced a spatially uniform distribution of dipole-forming O-Li bonds.

4.5 Progression Review

(110) Boron-Doped Diamond Sample	Surface Treatment	Work Function (eV) Φ	NEA (eV) χ
BS3	Hydrogen	3.54 ± 0.02	-0.93 ± 0.02
BS1	Hydrogen	3.64 ± 0.02	-1.07 ± 0.02
	Oxygen-Lithium (cycle 1)	4.12 ± 0.1	-0.58 ± 0.1
	Oxygen-Lithium (cycle 3)	3.01 ± 0.05	-1.49 ± 0.05

Table 2: All BS1 and BS3 (110) BDD sample work function and NEA results over the progression of the project from various surface terminations and functionalisation treatments.

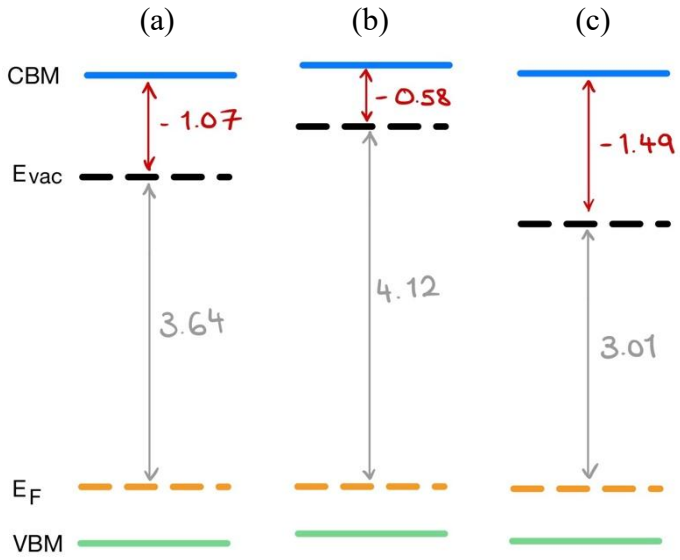

Figure 30: Band structure diagrams denoting work function and NEA values obtained from XPS, UPS, and EF-PEEM for the (a) hydrogen terminated surface, (b) 1st, and (c) 3rd molecular O-Li treatment cycles of the (110) BS1 BDD sample.

5. Conclusion

This project has demonstrated that controlled molecular oxygen and lithium functionalisation is an effective method for producing a low work function and negative electron affinity (NEA) on boron-doped single-crystal (110) diamond surfaces. A final work function of 3.01 ± 0.05 eV and NEA of -1.49 ± 0.05 eV were achieved following three cycles of oxygen-lithium treatment, representing a significant improvement over the hydrogen-terminated reference state work function of 3.64 ± 0.02 eV and NEA value of -1.07 ± 0.02 eV. When compared directly with previous University of Bristol studies for (110) diamond surfaces under similar treatment conditions, the present NEA results demonstrate excellent agreement [25] and, in respect to work function reduction, an improved performance [17], with the most significant improvement occurring after the third cycle due to increased O-Li bonding. This demonstrates that the (110) diamond orientation offers a reproducible method to produce large NEA and low work function surfaces. EF-PEEM mapping also confirmed that this reduction is spatially uniform, indicating the formation of a homogeneous, dipole-active surface.

These results contribute directly to the relatively limited body of work on the diamond (110) surface, demonstrating that iterative oxygen-lithium cycling can reliably tune its surface chemistry and electronic properties. The progression observed in the Li 1s and O 1s spectra shows that optimal NEA is achieved not through maximum oxygen coverage, but through the controlled formation of stable C-O-Li bonding.

The relatively low oxygen coverage of ~0.77% compared to previous studies of ~2% [25] after a singular exposure to molecular oxygen suggests that residual hydrogen may still play a limiting role, although the reduced hydroxyl contribution indicates that the implementation of a NEG may have improved vacuum conditions by limiting residual hydrogen re-adsorption. This highlights the continued importance of hydrogen management in achieving reproducible and optimised (110) surfaces. Future work should focus on improving oxygen incorporation and further suppressing hydrogen re-adsorption, with further investigation into using the NEG as a comparison study

Overall, this work establishes (110) diamond as a viable and tuneable platform for electron-emission applications, complementing the more widely studied (100) surface. Further investigations into density functional theory (DFT) calculations could be investigated to model the evolution of surface dipoles during oxygen-lithium cycling and predict optimal bonding configurations. Most importantly, applying the same molecular oxygen-lithium cycling process to the (100) diamond surface in future studies would enable a direct comparison of orientation-dependent behaviour and may yield even larger NEA values, given the higher oxygen uptake typically observed on (100) surfaces.

References

1. M. F. Campbell, T. J. Celenza, F. Schmitt, J. W. Schwede, I. Bargatin, *Progress Toward High Power Output in Thermionic Energy Converters*, Adv. Sci., **8**, 2003812 (2021) URL

2. A. Oriakhi, O. Okpako, E. Ikegwuonu, E. Aburime, S. Aliu, O. Ighodaro, H. Egware, M. Osikhuemhe, E. Omo-Oghogho, P. Akhator, U. Onochie, O. Unuareokpa, J. Achebo, C. Kwasi-Effah, *A Review of Energy Storage Technologies and Hybrid Configurations for Renewable-Integrated Power Systems,* NIPES - Journal of Science and Technology Research, **8**, 49-91 (2026) URL

3. A. Sharma, *Energy Harvesting Using Photovoltaic and Betavoltaic Devices* (Louisiana Tech University) (2016) URL

4. P. Rappaport, *The Electron-Voltaic Effect in p-n Junctions Induced by Beta-Particle Bombardment*, American Physical Society. **93,** 1, 246-247 (1954) URL

5. M. Prelas, C. Weaver, M. Watermann, E. Lukosi, R. Schott, D. Wisniewski, *A review of nuclear batteries. Progress in Nuclear Energy*, **75**, 117-148 (2014) URL

6. B. Harding, *Fabrication and Evaluation of P-i-N Diamond Betavoltaic Diodes*, MSci Thesis, University of Bristol (2025) URL

7. F. Zhao, Y. He, B. Huang, T. Zhang, H. Zhu, A *Review of Diamond Materials and Applications in Power Semiconductor Devices.* Materials. **17**, 3437 (2024) URL

8. D. Ghasemabadi, H. Dizaji, & M. Abdollahzadeh, *Theoretical Study of Conventional Semiconductors as Transducers to Increase Power and Efficiency in Betavoltaic Batteries* (2023) URL

9. M. James, F. Fogarty, R. Zulkharnay, N. Fox, & P. May, *A Review of Surface Functionalisation of Diamond for Thermionic Emission Applications.* Carbon. **171**, 532-550 (2021) URL

10. F. Fogarty, N. A. Fox & P. W. May, *Experimental studies of electron affinity and work function from titanium on oxidised diamond (100) surfaces*, Functional Diamond, **2**(1), 103-111 (2022) URL

11. R. Zulkharnay, P. W. May, *Experimental evidence for large negative electron affinity from scandium-terminated diamond*, J. Mater. Chem. A, **11**, 13432-13445 (2023) URL

12. K. W. Wong, Y. M. Wang, S. T. Lee, R. W. M. Kwok, *Negative electron affinity on polycrystalline diamond surface induced by lithium fluoride deposition,* Diamond and Related Materials, **8**(10), 1885-1890 (1999) URL

13. D. M. Trucchi, N. A. Melosh, *Electron-emission materials: Advances, applications, and models,* MRS Bulletin, **42**(7), 488-492, (2017) URL

14. V.S. Bormashov, S.Y. Troshiev, S.A. Tarelkin, A.P. Volkov, D.V. Teteruk, A.V. Golovanov, M.S. Kuznetsov, N.V. Kornilov, S.A. Terentiev, V.D. Blank, *High power density nuclear battery prototype based on diamond Schottky diodes,* Diamond and Related Materials. **84** (2018) URL

15. F. J. Himpsel, J. A. Knapp, J. A. Van Vechten, D. E. Eastman, Q*uantum photoyield of diamond (111)—a stable negative-affinity emitter*, Physical Review B, **20**, 624-627 (1979)

16. R. Zulkharnay & P. W. May, *Applications of diamond films: a review, Functional Diamond*, **4**:1, 2410160 (2024) URL

17. C. J. Brown, *Enhancement of negative electron affinity on the diamond (110) surface by cyclic low pressure molecular oxygen treatment and lithium deposition*, University of Bristol (2025)

18. D. Takeuchi, S.-G. Ri, H. Kato, C. E. Nebel, S. Yamasaki, *Negative electron affinity on hydrogen terminated diamond*, physica status solidi (a), **202**(11), 2098-2103 (2005) URL

19. D. Takeuchi, M. Riedel, J. Ristein, L. Ley, *Surface band bending and surface conductivity of hydrogenated diamond,* Physical Review B, **68**:041304 (2003) URL

20. R. Zulkharnay, W. Greenwood, A. Wood, J. Laverock, N. A. Fox, Achieving a Large Net "Negative Electron Affinity" on Diamond (100) via Molecular Oxygen and Lithium Functionalization, ACS Appl. Mater. Interfaces, **18**, 9032−9042 (2026) URL

21. K. M. O'Donnell, T. L. Martin, N. A. Fox, D. Cherns, *Ab initio investigation of lithium on the diamond C(100) surface*, Phys. Rev. B, **82** (11), No. 115303 (2010) URL

22. K. M. O'Donnell, T. L. Martin, N. L. Allan, *Light metals on oxygen-terminated diamond (100): Structure and electronic properties,* Chemistry of Materials, **27**(4), 1306–1315, 2015 URL

23. T.L. Martin, *Lithium oxygen termination as a negative electron affinity surface on diamond: a computational and photoemission study*, PhD Thesis, University of Bristol (2011) URL

24. R. Zulkharnay, G. Zulpukarova, P. May, *Oxygen-terminated diamond: insights into the correlation between surface oxygen configurations and work function values.* Applied Surface Science. **658** (2024) URL

25. B. Pritchard Cairns, *Optimising the true negative electron affinity of lithium-oxygen-terminated diamond (110)*, University of Bristol (2025) URL

26. P. W. May, *Diamond thin films: a 21st-century material*, Philosophical Transactions of the Royal Society of Londo, Series A: Mathematical, Physical and Engineering Sciences, **358**(1766), 473-495 (2000) URL

27. R. Zulkharney. *Electron emission studies of scandium on diamond for thermionic solar energy generation devices,* PhD Thesis, University of Bristol (2023) URL

28. K. Bobrov, H. Shechter, M. Folman, A. Hoffman, *A study of deuterium interaction with diamond (110) single crystal surface by TPD, EELS and LEED*, Diamond and Related Materials, Volume **8,** Issues 2-5, Pages 705-711 (1999) URL

29. F. Maier, R. Graupner, M. Hollering, L. Hammer, J. Ristein, L. Ley, *The hydrogenated and bare diamond (110) surface: a combined LEED-, XPS-, and ARPES study*, Surface Science, Volume **443**, Issue 3, Pages 177-185 (1999) URL

30. X. Li, J. Wei, J. Gao, Y. Wang, Y. Ma, P. An, S. Yu, K. Zheng, *Synergistic Control of Crystal Planes and Defects in CVD Single-Crystal Diamond: A Review of GrowthMechanisms and Frontier Applications,* Coatings, **16**, 218 (2026) URL

31. D. Takeuchi, H. Kato, G. Ri, T. Yamada, P. Vinod, D. Hwang, C. Nebel, H. Okushi, S. Yamasaki, *Direct observation of negative electron affinity in hydrogen-terminated diamond surfaces.* Applied Physics Letters. **86**, 152103-152103 (2005) URL

32. O.A. Williams, M.D. Whitfield, R.B. Jackman, J.S. Foord, J.E. Butler, C.E Nebel, *Formation of shallow acceptor states in the surface region of thin film diamond,* Applied Physics Letters, **78**(22), 3460-3462 (2001) URL

33. Y. Gong, W. Jia, B. Zhou, K. Zheng, D. Ma, Z. Li, J. Gao, Y. Ma, H. Hei, S. Yu, Y. Xue, Y. Wu, *Effect of boron doping levels on the microstructure and characteristics of high-quality boron-doped diamond electrodes prepared by MPCVD,* Diamond and Related Materials, Volume **139** (2023) URL

34. A. Fujishima, Y. Einaga, T. N. Rao, D. A. Tryk, *Diamond Electrochemistry*, Elsevier, Amsterdam (2005) URL

35. A. Einstein, *Über einen die Erzeugung und Verwandlung des Lichts betreffenden heuristischen Gesichtspunkt*, Annalen der Physik, **322**, 132 - 148 (2006)

36. M. Riffat, *X-Ray Photoelectron Spectroscopy Techniques* (2022) URL

37. K. M. O'Donnell, T. L. Martin, M. T. Edmonds, A. Tadich, L. Thomsen, J. Ristein, C. I. Pakes, N. A. Fox, L. Ley, *Photoelectron emission from lithiated diamond*, Feature Article, physica status solidi (a) **211**(10), 2209-2222 (2014) URL

38. M. P. Seah, W. A. Dench, *Quantitative electron spectroscopy of surfaces: A standard data base for electron inelastic mean free paths in solids,* Wiley (1979) URL

39. A. Croot, G. Wan, A. Rowan, H. D. Andrade, J. A. Smith, N. A. Fox, *Beta Radiation Enhanced Thermionic Emission from Diamond Thin Films*, Sec. Thermal and Mass Transport, Volume **3**, University of Bristol (2017) URL

40. R.K. Bhogal, *A Review of Functionalizing Diamond Surfaces for Thermionic Applications,* MSci Thesis, University of Bristol (2025) URL

41. R. Zulkharnay, N. A. Fox, P. W. May, *Enhanced Electron Emission Performance and Air-Surface Stability in ScO-Terminated Diamond for Thermionic Energy Converters,* Small, **20**(48) (2024) URL

42. W. Mönch, *Semiconductor Surfaces and Interfaces*, (Springer) (2001) URL

43. A. K. Tiwari, J. P. Goss, P. R. Briddon, N. G. Wright, A. B. Horsfall, R. Jones, H. Pinto, M. J, Rayson, *Calculated electron affinity and stability of halogen-terminated diamond*, Physical Review B, **84**, 245305 (2011) URL

44. S. Chaudhuri, S. Hall, B. Klein, M. Walker, A. Logsdail, J. Macpherson, R. Maurer, *Coexistence of carbonyl and ether groups on oxygen-terminated (110)-oriented diamond surfaces,* Communications Materials. **3** (2022) URL

45. J. Gracio, Q. Fan, & J. Mendes, *Diamond growth by chemical vapour deposition.* Journal of Physics D: Applied Physics. **43**, 374017 (2010) URL

46. F. Maier, J. Ristein, J. & L. Ley, *Electron affinity of plasma-hydrogenated and chemically oxidized diamond (100) surfaces*, Phys. Rev. B. **64**, 165411 (2001) URL

47. J. Phillip, M.D. Stoikou, *Hydrogen plasma interaction with (100) diamond surfaces*, The Royal Society of Chemistry, Vol. **13** (2011) URL

48. T. Martin, K. O'Donnell, H. Shiozawa, C. Giusca, N. Fox, S.R. Silva, & D. Cherns, *Lithium monolayers on single crystal C (100) oxygen-terminated diamond.* Materials Research Society symposia proceedings. Materials Research Society. 1282 (2011) URL

49. J. Angus, & C. Hayman, *Low-Pressure Metastable Growth of Dimaond and Diamond-Like Phases.* Science (New York, N.Y.). **241**, 913-21 (1988) URL

50. S. Kumaragurubaran, T. Yamada, S. Shikata, *Annealing effects in H- and O-terminated P-doped diamond (111) surfaces,* Diamond and Related Materials, Volume **17**, Issues 4-5, Pages 472-475 (2008) URL

51. *Sample Preparation*, School of Physics, University of Bristol, Website: https://www.bristol.ac.uk/physics/facilities/nanoesca/resources/sample-preparation/ [Accessed March 2026]

52. J. Ristein, *The Physics of Hydrogen-Terminated Diamond Surfaces*, AIP Conf. Proc. 772, 377-380 (2005) URL

53. P. C. Pinto, *History and potential of Non Évaporable Getter (NEG) Technology,* Workshop on Advanced Materials and Surfaces, CERN (2013)

54. J. F. Watts, J. Wolstenholme, *An Introduction to Surface Analysis by XPS and AES* (2003) URL

55. M. Escher, N. Weber, M. Merkel, B. Krömker, D. Funnemann, S. Schmidt, F. Reinert, F. Forster, S. Hüfner, P. Bernhard, C. Ziethen, H. Elmers, & G. Schönhense, *NanoESCA: imaging UPS and XPS with high energy resolution.* Journal of Electron Spectroscopy and Related Phenomena. **144**, 1179-1182 (2005) URL

56. J. E. Whitten. *Ultraviolet photoelectron spectroscopy: Practical aspects and best practices*, Applied Surface Science Advances, 13:100384 (2023) URL

57. M. G. Helander, M. T. Greiner, Z. B. Wang, Z. H. Lu, *Pitfalls in measuring work function using photoelectron spectroscopy*, Applied Surface Science, Volume **256**, Issue 8, Pages 2602-2605 (2010) URL

58. B.P. Tonner, D. Dunham, T. Droubay, M. Pauli, *A photoemission microscope with a hemispherical capacitor energy filter*, Journal of Electron Spectroscopy and Related Phenomena, **84**(1-3), 211–229 (1997) URL

59. G. Xiong, A. Joly, W. Hess, C. Mingdong, & T. Dickinson. *Introduction to Photoelectron Emission Microscopy: Principles and Applications.* Journal of Chinese Electron Microscopy Society. **25** (2006) URL

60. U. Scheithauer, G. Meyer, Gerhard & M. Henzler, *A new LEED instrument for quantitative spot profile analysis.* Surface Science. **178**, 441-451 (1986) URL

61. S. Ullah, L. Cullingford, T. Zhang, J. R. Wong, G. Wan, M. Cattelan, N. Fox, *An investigation into the surface termination and near-surface bulk doping of oxygen-terminated diamond with lithium at various annealing temperatures*, MRS Advances **6**, 311-320 (2021) URL

62. H. A. Girard, N. Simon, D. Ballutaud, A. Etcheberry, *Correlation between flat-band potential position and oxygenated termination nature on boron-doped diamond electrodes*, Comptes Rendus Chimie, **11**(9), 1010-1015 (2008) URL

63. L Diederich, O.M Küttel, P Aebi, L Schlapbach, *Electron emission and NEA from differently terminated, doped and oriented diamond surfaces*, Diamond and Related Materials, Volume **8**(2–5), 743-747 (1999) URL

64. L. Diederich, O.M. Küttel, P. Aebi, L. Schlapbach, *Electron affinity and work function of differently oriented and doped diamond surfaces determined by photoelectron spectroscopy*, Surface Science, **418**(1), 219-239 (1998) URL

65. M. De La Pierre, M. Bruno, C. Manfredotti, F. Nestola, M. Prencipe, C. Manfredotti, *The (100), (111) and (110) surfaces of diamond: an ab initio B3LYP study,* Molecular Physics: An International Journal at the Interface Between Chemistry and Physics, **112**:7 (2014) URL

66. P.K. Baumann 1, R.J. Nemanich, *Surface cleaning, electronic states and electron affinity of diamond (100), (111) and (110) surfaces, Surface Science,* **409**, 320-335 (1998) URL

Appendix

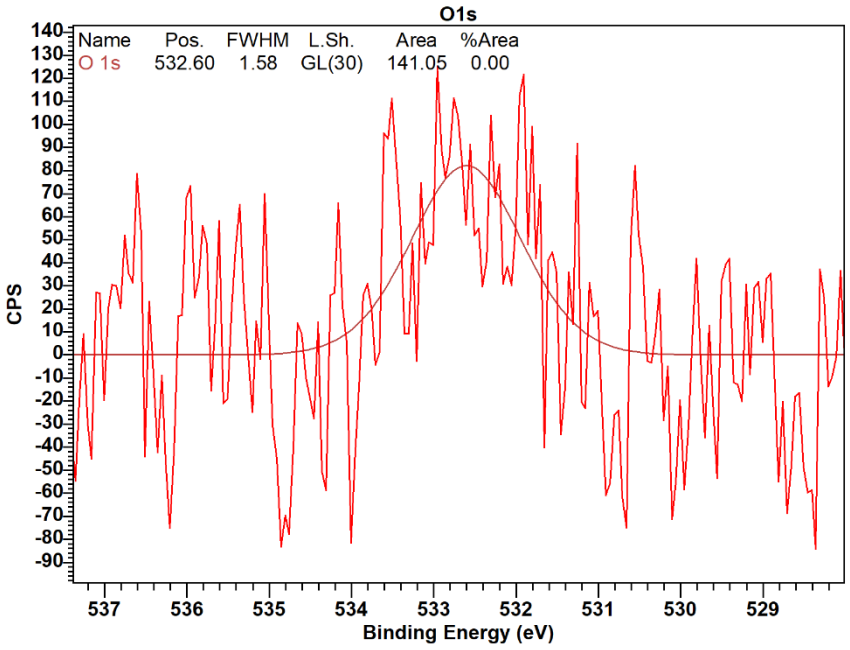

Figure 1: Fitted core-level XPS.2 spectra of the O 1s peak following a 900 °C anneal for the (110) BS1 BDD sample. Original spectra of the collected XPS data shown in bright red, with fitted chemical components colour coded by the key shown in figure. sp^3 C-C (B) and sp^3 C-C (S) represent 'Bulk' and 'Surface' C-C bonds, respectively.

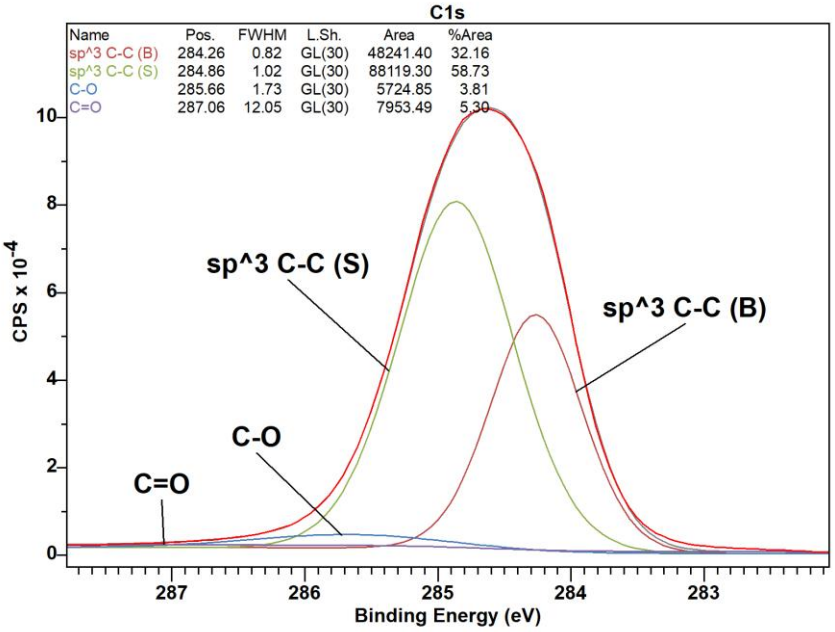

Figure 2: Fitted core-level XPS.2 spectra of the C 1s peak following a 900 °C anneal for the (110) BS1 BDD sample. Original spectra of the collected XPS data shown in bright red, with fitted chemical components colour coded by the key shown in figure. sp^3 C-C (B) and sp^3 C-C (S) represent 'Bulk' and 'Surface' C-C bonds, respectively.

Certification of ownership of the copyright

This Project Report is presented as part of, and in accordance with, the requirements for the degree of MSci at the University of Bristol, Faculty of Science.

Author	Sophie Kelly
Title	An investigation into refining the negative electron affinity and work function of boron-doped (110) diamond surfaces via oxygen-lithium treatments
Date of submission	13/04/2026